Cavity-QED measurements of the ^{87}Sr millihertz optical clock transition and determination of its natural linewidth

Juan A. Muniz,* Dylan J. Young, Julia R. K. Cline, and James K. Thompson
JILA, NIST, and Department of Physics, University of Colorado, 440 UCB, Boulder, Colorado 80309, USA

(Received 18 July 2020; revised 22 January 2021; accepted 15 April 2021; published 27 May 2021)

We demonstrate the direct quantum nondemolition detection of a millihertz linewidth optical atomic transition. We observe the modification of the phase and amplitude of a probe field interacting with strontium atoms, which provides a direct spectroscopic signal to which a laser could be frequency stabilized. To investigate this measurement capability, we demonstrate an approach to determining the intrinsic natural lifetime of exceptionally long-lived optical excited states. Such transitions are key to the performance of state-of-the-art atomic clocks, have potential applications in searches for fundamental physics and gravitational wave detectors, as well as quantum many-body phenomena. Here, we determine the ratio of the challenging to measure and poorly known ultranarrow linewidth transition ($^3P_0$ to $^1S_0$ in ^{87}Sr) to that of another narrow well-known transition ($^3P_1$ to $^1S_0$) by coupling the two transitions to a single optical cavity and performing interleaved nondestructive measurements of the interaction strengths of the atoms with cavity modes near each transition frequency. We use this approach to determine the natural linewidth of the clock transition $^3P_0$ to $^1S_0$ in ^{87}Sr to be $\gamma_0/(2\pi) = 1.35(3)$ mHz or $\tau = 118(3)$ s. The 30-μHz resolution implies that we could detect states with lifetimes just below 2 h, and with straightforward future improvements, we could detect states with lifetimes up to 15 h, using measurement trials that last only a few hundred milliseconds, eliminating the need for long storage times in optical potentials. This work opens the path to nondestructive direct spectroscopy of ultranarrow transition for continuous frequency measurements and laser stabilization.

DOI: 10.1103/PhysRevResearch.3.023152

I. INTRODUCTION

Ultranarrow linewidth optical transitions have become the new standard for precision optical metrology, providing fast phase evolution, long coherence times, and intrinsic insensitivity to key environmental perturbations that have allowed remarkable fractional accuracy at the 10^{-18} level [1–8]. They have a wide range of potential applications for fundamental physics, such as gravitational wave detection using matter-wave interferometry or dark-matter searches [9–16], quantum many-body physics [17–22], novel cavity QED applications for superradiant lasing [23,24], and spin squeezing on an optical clock transition [25].

Here, we demonstrate the direct quantum nondemolition detection of a millihertz linewidth optical transition by the observed modification of the phase and amplitude of the probe field that interacts with the atoms on the ultranarrow transition. This observation provides a direct spectroscopic signal to which a laser could in principle be frequency stabilized [26], with previous analogous observations on the 10^7 times broader 7.5-kHz transition in strontium [27–29]. Our technique contributes towards the aim of creating a different type of atomic clock built with optical cavities that is complementary to traditional discretely sampled atomic clocks based on Ramsey and Rabi spectroscopy and offers enhanced measurement bandwidth and similar predicted sensitivities to superradiant lasers [24,30–32]. Increased bandwidth would reduce the challenging requirements on local oscillators and would enhance the bandwidth for searches for dark matter or other new fields [15], for example. The nondestructive readout of atomic populations will also reduce the problem of Dick noise aliasing in traditional atomic clocks that rely on destructive readout. Compared with previous work that probed kHz to MHz linewidth transitions [25,33–39], our work probes an ultranarrow optical transition with a millihertz-level linewidth.

We explore and apply this detection capability to determine the fundamental intrinsic linewidth of the ultranarrow clock transition, which is important for understanding the ultimate limits on quantum coherence offered by various atomic transitions and species. Although the expected lifetime of long-lived excited states can surpass 100 s [40–47], various competing processes can preclude the observation of the natural excited-state lifetime, such as black-body radiation-induced decay [40,48] or scattering due to optical lattice light used to trap the atoms [49–51], preventing the application of standard population decay techniques to determine their lifetimes. For example, state-of-the-art optical lattice clocks have only demonstrated coherence up to ∼10 s [3,50,51]

*Present address: Instituto de Física, Facultad de Ingeniería, Universidad de la República, J.H. y Reissig 565, 11300 Montevideo, Uruguay; jmunizq2@gmail.com

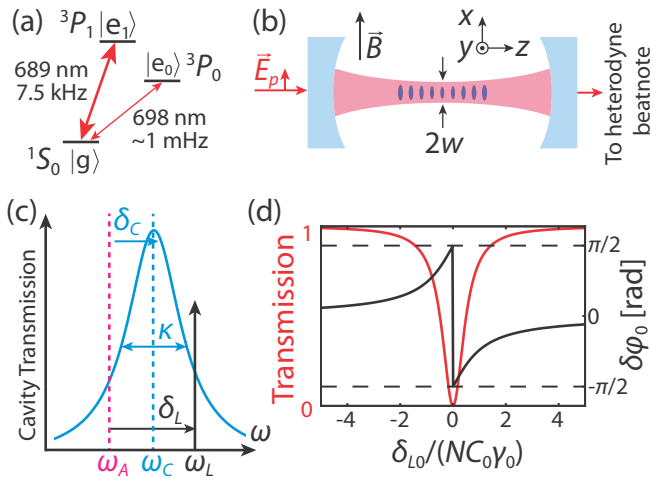

FIG. 1. System description. (a) Relevant energy levels in ^{87}Sr. (b) Atoms are trapped inside an intracavity optical lattice. The probe electric field $\vec{E}_p$ is polarized along the magnetic field $\vec{B}$ direction ($\hat{x}$) and has mode waist radius w. Phase detection is done via heterodyne measurements. (c) Experimental frequencies showing the cavity center frequency ω_C, laser frequency ω_L, and their respective detunings δ_C and δ_L from the atomic transition frequency ω_A. Light leaks out of the cavity at a total rate κ. (d) For the clock transition (subindex 0), simulated cavity transmission and phase shift $\delta\varphi_0$ against probe detuning δ_{L0} for $\delta_{C0} = 0$ in units of $NC_0\gamma_0$. At a given detuning, the phase shift produced by the atomic ensemble is proportional to γ_0.

which is limited mostly by Raman scattering of the lattice light off an excited state [50]. In fact, most of the systems where these long excited-state lifetimes have been precisely measured consist of atoms trapped without optical potentials, such as magnetic or ion traps [40–47], and in some nondestructive detection has been performed [52].

To date, the two reported values for the $^3P_0$ excited-state lifetime in ^{87}Sr are $\tau = 330(140)$ s from Ref. [49] obtained from population decay measurements from excited metastable states, and $\tau = 145(40)$ s from Ref. [53] obtained from effective atomic models and measurements of differential Landé g factors between ground and excited clock states, while *ab initio* calculations estimate a lifetime between 110–130 s [54,55]. With the implementation of new potential landscapes for operating with reduced lattice-induced scattering [50,56,57] that can suppress these effects, and with reference optical cavities whose coherence times start to approach the minute timescale [58–60], the full enhancement of these ultranarrow optical transitions can be achieved.

In this paper, we present a series of cavity-enhanced spectroscopic measurements directly on the ^{87}Sr clock transition. This technique allows us to directly determine the natural lifetime of the excited clock state $^3P_0$ ($|e_0\rangle$) in ^{87}Sr. Our technique consists of precisely and simultaneously measuring the *ratio* of single-photon Rabi frequencies along two optical transitions, the millihertz transition ($^1S_0 = |g\rangle \rightarrow {}^3P_0 = |e_0\rangle$) and the 7.5-kHz transition ($^1S_0 \rightarrow {}^3P_1 = |e_1\rangle$), using a common atomic ensemble inside an optical resonator [see Fig. 1(a)]. These single-photon Rabi frequencies, denoted by $2g_{0,1}$ for light-matter coupling strengths along the millihertz and 7.5-kHz transitions, respectively, depend on the electric dipole moment of the atoms (d) along with well-known and independently characterized geometric factors [61], such as the cavity's mode waist (w) and length (L). The natural linewidth γ_0 can then be linked to the known natural linewidth γ_1 from the measured coupling strength ratio as

$$\frac{\gamma_0}{\gamma_1} = \left(\frac{\mathrm{L}_0}{\mathrm{L}_1}\right)\left(\frac{\mathrm{w}_0}{\mathrm{w}_1}\right)^2\left(\frac{\omega_{A0}}{\omega_{A1}}\right)^2\left(\frac{g_0}{g_1}\right)^2, \tag{1}$$

where ω_A is the (well-known) atomic transition frequency. Note that, for this paper, we generically use subscripts 0 and 1 to denote quantities for the clock transition (with wavelength $\lambda_0 = 698.44$ nm) and the 7.5-kHz transition (with wavelength $\lambda_1 = 689.45$ nm) respectively, as shown in Fig. 1(a). Calculating this ratio as opposed to just the millihertz transition Rabi frequency allows for the cancellation of many common noise and systematic effects such as atom-number fluctuations, inhomogeneous atom-cavity coupling, cavity and laser frequency noise, and finite-ensemble-size effects.

II. DISPERSIVE MEASUREMENTS USING NARROW OPTICAL TRANSITIONS

To accomplish the above, we perform consecutive measurements of the dispersive cavity resonance frequency shift $\Delta\omega_1$ (or equivalently the multipass phase shift $\Delta\varphi_1$) on the 7.5-kHz transition, as well as the dispersive phase shift $\Delta\varphi_0$ on the millihertz transition. These phase shifts depend directly on the light-matter coupling strength, scaling as $\Delta\varphi_0/\Delta\varphi_1 \propto (g_0/g_1)^2$ [62,63].

Ultimately, this involves measuring the phase shift experienced by far off-resonant light passing through an atomic medium [Fig. 1(b)], which arises from the interference between the incident and the scattered fields. The optical cavity magnifies this phase shift due to the multiple round trips [61] and defines the spatial modes that interact with the atoms. An optical resonator also introduces systematic effects that we take into account later in this paper. Remarkably, due to the ultranarrow linewidth of the clock transition, our phase shift measurements $\Delta\varphi_0$ are dispersive, i.e., the probe is sufficiently detuned from the atomic transition, while also being in the resolved motional sideband limit, as the axial vibration frequency is much larger than the probe's detuning. This scenario does not have precedent in the atomic quantum nondemolition (QND) measurements community.

Our system, also described in [23,24], consists of an ensemble of up to 10^5 ^{87}Sr atoms confined within a high-finesse optical cavity by a $\lambda_{\mathrm{trap}} = 813$ nm, near-magic wavelength intracavity optical lattice, as sketched in Fig. 1(b) [3,64]. We optically pump the atoms into a 50/50 spin mixture of the $^1S_0$ nuclear Zeeman levels $m_F = \pm\frac{9}{2}$, with less than 5% of atoms remaining in the other 8 m_F states. The 813-nm trap is 185 μK deep, with measured axial trap frequency $\omega_z/(2\pi) = 230(1)$ kHz. The atoms have an axial temperature $T_z = 14(1)$ μK, and their mean vibrational quantum number is $\bar{n}_z = 0.9(1)$, obtained using sideband spectroscopy [65].

Both transitions fall into the so-called bad cavity regime, where the ~150-kHz cavity linewidth (κ) is larger than the excited-state linewidth (γ). To understand the dispersive measurements we perform, we consider N equally coupled

two-level atomic dipoles with transition frequency ω_A that interact with one cavity mode at frequency ω_C, detuned by $\delta_C = \omega_C - \omega_A$ from the atomic transition, as shown in Fig. 1(c).

For the 7.5-kHz transition our system typically satisfies $NC_1\gamma_1 \gg \kappa_1$, with $C_1 = (2g_1)^2/(\gamma_1\kappa_1)$ denoting the single-atom cooperativity parameter that characterizes the cavity-enhanced interactions on this transition [63,66]. This gives a resolved collective vacuum Rabi splitting for a resonant cavity mode ($\delta_{C1} = 0$). For this experiment, we instead operate in the dispersive limit ($\delta_{C1} \gg \sqrt{N}g_1$), where the cavity resonance frequency experiences a shift $\delta\omega_1 = Ng_1^2/\delta_{C1}$ [66] due to the presence of N atoms in the ground state. This frequency shift corresponds to an equivalent multipass phase shift $\delta\varphi_1 = \delta\omega_1/(\kappa_1/2) = NC_1\gamma_1/2\delta_{C1}$. This regime has been explored in many different QND platforms [67–73].

Dispersive measurements on the ^{87}Sr millihertz transition

The millihertz optical transition falls into a less common regime for ensemble-cavity experiments, where the collective vacuum Rabi splitting is unresolved and $NC_0\gamma_0 \ll \kappa_0$, with $C_0 = (2g_0)^2/(\gamma_0\kappa_0)$ the single-atom cooperativity parameter. Dispersive measurements are realized by observing the multipass phase shift $\delta\varphi_0$ of the transmitted probe light detuned δ_{L0} from the atomic transition ω_{A0}. In this case $\delta\varphi_0 = -NC_0\gamma_0/(2\delta_{L0}) - (\delta_{C0} - \delta_{L0})/(\kappa_0/2)$ for small angles [$\kappa_0 \gg (\delta_{C0}, \delta_{L0}) \gg NC_0\gamma_0$]. The first term that contributes to $\delta\varphi_0$ is the phase shift induced on the probe light by the atoms, the quantity that we wish to measure. The second term is a phase shift that arises when the probe light is not on resonance with an empty cavity, representing a background that must be subtracted.

The normalized power transmission (red line) and phase shift $\delta\varphi_0$ (black line) for a weak probe in the presence of atoms for $\delta_{C0} = 0$ are shown in Fig. 1(d). In the weak excitation limit, the transmission drops as the incident and scattered electric fields destructively interfere over a characteristic frequency width of order $NC_0\gamma_0$, while $\delta\varphi_0$ shows a narrow feature around $\delta_{L0} = 0$ of order γ_0. As $|\delta_{L0}|$ increases, the cavitylike phase shift starts to be significant compared to the atomiclike phase shift: for our chosen probe detuning $|\delta_{L0}|/(2\pi) = 1$ kHz, the former is ∼15 mrad while the latter is ∼40 mrad.

To measure $\delta\varphi_0$ we select a TEM$_{00}$ cavity mode and adjust the cavity length to be on resonance with the clock transition, i.e., $\delta_{C0} = 0$. At the clock transition wavelength λ_0, the cavity's linewidth is $\kappa_0 = 2\pi \times 140.9(3)$ kHz, while the free spectral range (FSR) is $\Delta_{\mathrm{FSR},0} = 2\pi \times 3.714\,61(3)$ GHz. The different probe tones used to determine the phase shifts $\delta\varphi_{0,1}$ are created using an in-fiber electro-optical phase modulator (EOM) before being coupled to the cavity, and are polarized along the quantization direction $\hat{x}$, established by a static magnetic field $\vec{B} = B_0\hat{x}$ with $B_0 \sim 100$ mG [Fig. 1(b)].

We investigate the cavity transmission characteristics in the presence of atoms for the ultranarrow transition in Fig. 2, observing spectroscopic signals that could be used in the future for stabilization of a laser to the atomic transition frequency, providing an atomic clock with complementary properties to traditional atomic clocks. The atomic clock

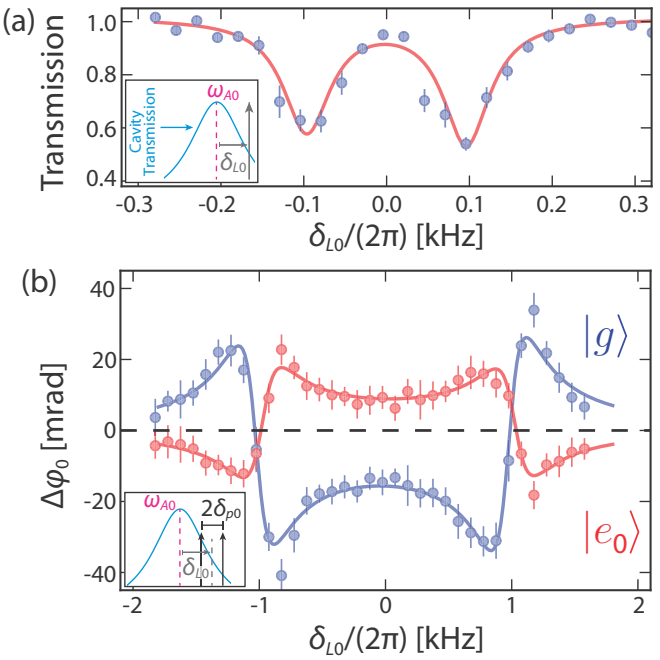

FIG. 2. Probing the clock transition. (a) Transmitted power for a single tone versus its detuning δ_{L0} from the narrow clock transition frequency ω_{A0} (see inset). The two dips correspond to atoms in the ground $m_F = \pm 9/2$ states in the presence of a 200-mG magnetic field that creates a 200-Hz nuclear Zeeman splitting in the optical transition frequency. (b) Atomic-induced phase shift $\Delta\varphi_0$ on the clock transition as the central frequency detuning δ_{L0} of the probes from the clock transition frequency ω_{A0} is scanned (see inset). The probes are detuned $2\delta_{p0}/(2\pi) = 2$ kHz from each other. Blue (red) markers are for atoms initially in $|g\rangle$ ($|e_0\rangle$). Solid lines are empirical fits that take into account the finite excitation fraction. Either the transmitted probe amplitudes or phases could serve in the future as frequency references for laser frequency stabilization to an ultranarrow optical transition.

transition is addressed with light from a stabilized state-of-the-art sub-10-mHz linewidth laser [2,58,60]. The power transmission of a near-resonant probe, detuned by δ_{L0} from the atomic transition, exhibits two distinct peaks [Fig. 2(a)], associated with the $m_F = \pm\frac{9}{2}$ ground states in the presence of a magnetic field [53]. We attribute the absence of full absorption in this example data to an overly large probe power causing atoms to transition to the excited state $^3P_0$. The imbalance in the depth of the absorption features is attributed to imbalance on the relative $m_F = \pm\frac{9}{2}$ populations.

To gain partial immunity to systematic uncertainty in the atomic transition frequency (i.e., uncertainty in δ_{L0}) as well as laser frequency noise, we probe the cavity with two symmetrically detuned tones at $\delta_{L0} \pm \delta_{p0}$ and measure their phase shifts, i.e., $\delta\varphi_0(\delta_{L0} \pm \delta_{p0})$, by creating a heterodyne beat note. Typically, $\delta_{p0}/(2\pi) = 1$ kHz. The *difference* between these two phases encodes the atomic contribution that we would like to measure. To extract this atomic contribution and further reduce sensitivity to various sources of frequency noise, we simultaneously measure the phase shift of an identical pair of tones that probe a consecutive TEM$_{00}$ cavity mode [$\delta\varphi_0(\Delta_{\mathrm{FSR},0} + \delta_{L0} \pm \delta_{p0})$]. Finally, we compute the *pairwise*

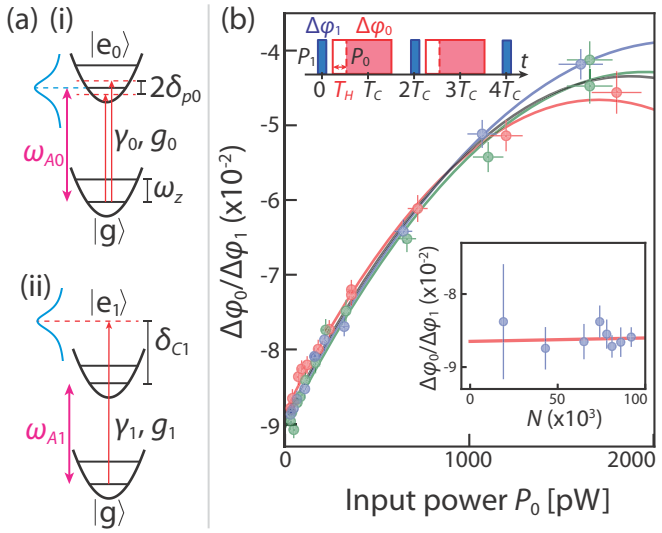

FIG. 3. Measuring (g_0/g_1). (a) (i) For the phase shift measurement $\Delta\varphi_0$, the two probe tones are detuned by only 1 kHz from the atomic transition, to be compared to the spacing between the axial motional levels $\omega_z/(2\pi) = 230$ kHz. In this resolved-sideband regime, the probe tones experience a differential phase shift primarily from the carrier transition that does not change the motional quantum number. Due to finite axial confinement, the carrier transition strength is reduced by 6%, the largest correction factor that must be applied to our measurement. (ii) In contrast, for the phase shift measurement $\Delta\varphi_1$ the probe tones are far detuned and the probe experiences a phase shift due to interacting with all motional sideband transitions. (b) Ratio $\Delta\varphi_0/\Delta\varphi_1$ measurement, from the interleaved pulse sequence (top inset) as P_0 is changed. Different colors correspond to different measurement sets (markers), over different days, and their color matching solid lines are quadratic polynomial fits on P_0 according to our model discussed in Appendix E. Statistical errors (1σ) are indicated by the error bars. Top inset shows the measurement sequence, which alternates three 2-ms $\Delta\varphi_1$ measurements between two 25-ms $\Delta\varphi_0$ measurements (first $T_H = 5$ ms are removed for the extraction of $\Delta\phi_0$). The solid black line is a global fit to the three measurements. The bottom inset shows $\Delta\varphi_0/\Delta\varphi_1$ (markers) and its weighted linear fit (solid line), for a fixed set (P_0, P_1), as atom number N is changed.

difference $\Delta\varphi_0 = [\delta\varphi_0(\delta_{L0} + \delta_{p0}) - \delta\varphi_0(\delta_{L0} - \delta_{p0})] - [\delta\varphi_0(\Delta_{\mathrm{FSR},0} + \delta_{L0} + \delta_{p0}) - \delta\varphi_0(\Delta_{\mathrm{FSR},0} + \delta_{L0} - \delta_{p0})]$. For the rest of the paper $\Delta\varphi_0$ refers to this quantity. Note that on resonance $(\delta_{L0} = 0)$ the phase shift is $\Delta\varphi_0 = -NC_0\gamma_0/\delta_{p0}$.

In Fig. 2(b) we measure $\Delta\varphi_0$ against δ_{L0} for atoms initially in $|g\rangle$ when the two symmetric tones are applied (blue markers). The sharp resonances near $\delta_{L0} = \pm\delta_{p0}$ occur when one of the tones is near resonant with the atoms, while for this magnetic field (∼100 mG) and probe power, the Zeeman level resonances are not resolved. Importantly, by using two tones, the measured phase shift is now only quadratically sensitive to the detuning δ_{L0} when $|\delta_{L0}| \ll \delta_p$. Furthermore, we measure $\Delta\varphi_0$ after having adiabatically transferred the atoms to $|e_0\rangle$ [23,24], and remove the remaining atoms in $|g\rangle$ using the strong $^1S_0$ - $^1P_1$ transition at 461 nm (red markers). We clearly observe $\Delta\varphi_0$ switching sign along with the atomic inversion $(N \to -N)$, as well as a reduction of the signal, in agreement with the measured adiabatic transfer efficiency. We note both sets seem to be shifted from one another in frequency by less than 100 Hz, the typical uncertainty to determine $\delta_{L0} = 0$. The change in sign of the signal illustrates that the observed phase shifts can be used to provide a differential readout of atomic populations in the ground and excited states for nondestructive readout of traditional Ramsey and Rabi spectroscopy or entanglement generation. The high-frequency resolution also means that dual simultaneous probing of two transitions at once can provide rejection of magnetic field noise.

III. LINEWIDTH MEASUREMENT OF THE ^{87}Sr $^1S_0 \to {}^3P_0$ TRANSITION

We now center our attention on the measurement of γ_0. In order to extract the ratio of linewidths γ_0/γ_1, we will need to measure the ratio of the squares of the two single-photon Rabi frequencies $(g_0/g_1)^2$ as described in Eq. (1). This quantity can be measured by comparing multipass phase shifts on the two transitions. Our strategy relies on measuring $\Delta\varphi_0$ when the cavity and probes' center frequency are on resonance with the millihertz atomic transition, i.e., $\delta_{C0} = \delta_{L0} = 0$, and the 7.5-kHz transition phase shift $\Delta\varphi_1$ in the same configuration with the same atomic ensemble. As the cavity length is already stabilized to be on resonance with the clock transition $(\delta_{C0} = 0)$, the closest cavity mode will be detuned by δ_{C1} from the 689-nm transition $|g\rangle \to |e_1\rangle$ [Fig. 3(a)(ii)]. The cavity linewidth at 689 nm is $\kappa_1/(2\pi) = 153.0(4)$ kHz.

We set the cavity length such that the closest mode to the excited $^3P_1$ $F' = \frac{9}{2}$ state is detuned by $\delta_{C1}/(2\pi) = 277.5(8)$ MHz. The cavity phase shift $\delta\varphi_1$ is computed by measuring the cavity frequency shift $\delta\omega_1$ of the TEM_{00} mode detuned by δ_{C1} from ω_{A1}. To probe $\delta\omega_1$, we scan the frequency of a weak π-polarized probe across the cavity resonance. As before, in order to gain further insensitivity with respect to cavity and laser frequency noise, we simultaneously probe a consecutive longitudinal TEM_{00} mode of the cavity at frequency $\delta_{C1} - \Delta_{\mathrm{FSR},1}$, and compute the *difference* $\Delta\varphi_1 = \delta\varphi_1(\delta_{C1}) - \delta\varphi_1(\delta_{C1} - \Delta_{\mathrm{FSR},1})$ (see Appendix B for details). From now on we will refer to $\Delta\varphi_1$ as this measured quantity.

Using phase shifts induced on probe light by ultranarrow transitions has previously been proposed for laser frequency stabilization [26,27] but in the saturated and resonant configuration, which is intrinsically destructive. Here, using joint measurements of the phase shifts $\Delta\varphi_0$ and $\Delta\varphi_1$ we can extract the ratio of light-matter coupling rates $(g_0/g_1)^2$ according to

$$\left(\frac{g_0}{g_1}\right)^2 = -\left(\frac{\Delta\varphi_0}{\Delta\varphi_1}\right)\left(\frac{\kappa_0}{\kappa_1}\right)\left(\frac{\delta_{p0}}{\delta_{C1}}\right), \tag{2}$$

allowing us to calculate γ_0 from the known γ_1 via Eq. (1). Our experimental scheme relies on nondestructive interleaved measurements of $\Delta\varphi_0$ and $\Delta\varphi_1$ during a single shot such that the inhomogeneity of the atom-cavity coupling [69,70] and fluctuations in atom number N are common to both measurements and cancel in the final computed ratio. In comparison with other methods, ours constitutes a nondestructive probe of the atomic inversion on the clock states, with the possibility to be used for continuous tracking of the inversion.

The ratio of $(g_0/g_1)^2$ is directly encoded in the $\Delta\varphi_0/\Delta\varphi_1$ measurement, absent atomic excitations, as described in Eq. (2), taking into account the details of the measurement

TABLE I. Largest identified corrections and uncertainties.

Effect	Affects	Correction
Finite axial confinement	$\Delta\varphi_0/\Delta\varphi_1$	1.062(4)
Cavity birefringence	$\Delta\varphi_0/\Delta\varphi_1$	1.012(5)
Atomic resonance uncertainty	$\Delta\varphi_0$	0.994(6)
Cavity resonance offset	$\Delta\varphi_0$	1.008(6)

and atomic structure. To approach the zero-power limit where no atomic excitations are created we measure $\Delta\varphi_0/\Delta\varphi_1$ as the probe optical powers are reduced. In order to gain insensitivity to atom loss from the lattice (lifetime about 500 ms), we alternate three short (∼2 ms) $\Delta\varphi_1$ measurements with two longer (∼25 ms) $\Delta\varphi_0$ measurements, as indicated in Fig. 3(b) top inset. From these five measurements we build a suitable estimator for the ratio $\Delta\varphi_0/\Delta\varphi_1$ and extract the ratio $(g_0/g_1)^2$.

Experimental results are shown in Fig. 3(b). Probe optical powers P_0 and P_1 for the 698- and 689-nm probes, respectively, are reduced to interpolate to the zero-power value for $\Delta\varphi_0/\Delta\varphi_1$. Three different measurement sets (markers) are shown for consistency and repeatability in Fig. 3(b), each fitted with a quadratic polynomial on P_0 (solid lines) with reduced χ^2_ν near 1 for all sets. For these data sets, we have verified that the P_1 was already sufficiently low to avoid creating excitations in $|e_1\rangle$ (see Appendices A and C for details). Each of these sets were taken on different days and with independent cavity alignments to the clock transition. A simultaneous fit to the three sets is shown as a solid black line in Fig. 3(c). Using different estimators and fit methods, we consistently measure a zero-power crossing ratio $(\Delta\varphi_0/\Delta\varphi_1)_{\rm exp} = -8.95(9)\times10^{-2}$.

We note that the spread of the zero-power values for different sets is consistent with the effect of the estimated uncertainty on our ability to tune δ_{C0} to zero for each data set. The bottom inset in Fig. 3(b) shows $\Delta\varphi_0/\Delta\varphi_1$ for different atom number N and a fixed powers P_0 and P_1, with the red line indicating a linear weighted fit. The variation of the measured values suggests that we can constrain any unknown first-order variation with N or N^{-1} to the 2% level, within our final uncertainty, limited by signal to noise. Since there is not an underlying model for why these scalings would exist (beyond offsets in $\Delta\varphi_0$ and $\Delta\varphi_1$ accounted for separately), no adjustment to the quoted uncertainty is applied.

Systematic corrections

To precisely determine the excited clock state linewidth from the measured $(\Delta\varphi_0/\Delta\varphi_1)_{\rm exp}$, several systematic effects need to be accounted for. A detailed description is given in Appendix D, but here we focus on a few corrections (Table I). The largest systematic correction that must be applied arises from the fact that the phase shift measurements $\Delta\varphi_0$ are made in a resolved sideband regime in which the probe detunings $\delta_{p0}/(2\pi) = \pm1$ kHz are much less than the axial trapping frequency $\omega_z/(2\pi) = 230(1)$ kHz, as shown in Fig. 3(a). To be in a dispersive regime requires $\delta_{p0} \gg NC_0\gamma_0$; for most fully allowed optical transitions, this typically implies $\delta_{p0} \gg \omega_z$ when $NC_0 \gg 1$. However, here γ_0 being so small allows us to operate in the dispersive regime, probing the carrier transition, even when $\delta_{p0} \ll \omega_z$. For our atomic sample, the correction to the measured $\Delta\varphi_0/\Delta\varphi_1$ is 1.062(4), where we also take into account the inhomogeneous coupling between probes and atoms across the optical lattice.

The cavity also possesses intrinsic birefringence which modifies both phase shifts and thus changes $\Delta\varphi_0/\Delta\varphi_1$. Rather than a single polarization-independent cavity resonance, birefringence creates two normal modes split by frequencies δ_{b0} and δ_{b1} at λ_0 and λ_1, respectively. If θ_b is the opening angle between the probe beam polarization ($\hat{x}$) and the birefringent eigenmode axis on the Poincaré sphere, the correction on each phase shift scales as $[\delta_{bi}/(\kappa_i/2)\sin\theta_b]^2$ for $i \in \{0, 1\}$. Including relevant measurement details, such as the hyperfine structure of the relevant states, imperfect state preparation in the ground-state hyperfine manifold, uncertainty in the polarization alignment of the local oscillator polarization relative to the probe's polarization, and possible differential linewidths for both birefringent normal modes, we determine a correction factor on the phase shift ratio of 1.012(5).

Furthermore, the atomic phase shift measurement $\Delta\varphi_0$ is quadratically sensitive to uncertainty in the detuning $\delta_{L0}/(2\pi) = 0 \pm 100$ Hz [Fig. 2(b)]. Corrections on the measured value of $\Delta\varphi_0$ from this effect scale as $[1-(\delta_{L0}/\delta_{p0})^2]$. Similarly, $\Delta\varphi_0$ depends quadratically on the cavity resonance condition, i.e., how close δ_{C0} is to 0. This correction scales as $[1+(\delta_{C0}/(\kappa_0/2))^2]$, where typically $|\delta_{C0}|/(2\pi) \lesssim 10$ kHz.

Considering all the other systematic effects studied in Appendix D, the correction factor to $(\Delta\varphi_0/\Delta\varphi_1)_{\rm exp}$ is $F_C = 1.074(16)$. The corrected ratio is then $\Delta\varphi_0/\Delta\varphi_1 = -9.61(17)\times10^{-2}$. In order to use the measured value for $\Delta\varphi_{0,1}$ to determine $(g_0/g_1)^2$ as in Eq. (2), we need to take into account the hyperfine structure in the $^3P_1$ state manifold, which would modify the expression for the associated phase shift $\Delta\varphi_1$. Following the discussion in the Appendix C, we extract $(g_0/g_1)^2 = 1.83(3)\times10^{-7}$. Finally, using Eq. (1) we determine $\gamma_0/\gamma_1 = 1.81(3)\times10^{-7}$, where the waist (w) and length (L) for each mode are independently characterized in our Appendix B following the treatment in [74]. Using the value of $\gamma_1/(2\pi) = 7.48(1)$ kHz measured in Ref. [75], we finally find $\gamma_0/(2\pi) = 1.35(3)$ mHz for the clock excited-state natural linewidth. This value implies an excited-state lifetime of $\tau_0 = 118(3)$ s, in agreement with Ref. [53] but in disagreement with Ref. [49]. *Ab initio* atomic structure calculations place the atomic linewidth at 1.4(5) mHz in Ref. [55], and 1.2 mHz in Ref. [54]. We also note that the value used for γ_1 reported in Ref. [75] is consistent with previous less precise determinations, with relative uncertainties at the 2% level, from decay and photoassociation measurements [76,77].

IV. CONCLUSIONS

In conclusion, we show that cavity-enhanced dispersive measurements can be used to realize spectroscopic measurements directly on ultranarrow optical transitions. We report state-dependent phase shifts on the ^{87}Sr clock transition, that are notably nondestructive, allowing for continuous tracking of the transition frequency and potentially allowing laser stabilization to these transitions. With further improvements on our detection setup, this scheme could be used as an atom counting tool directly on the clock transition, in contrast

to other systems [33–38]. This tool would be particularly useful for new optical lattice clocks built with optical cavities. Moreover, our setup represents a potential path for laser stabilization to ultranarrow lines such as in a continuous superradiant laser.

Finally, we report a lifetime resolution of 30 μHz, which implies we could determine excited-state lifetimes of up to 90 min in comparable integration time ∼100 ms. With reasonable improvements in our setup, we could expect to determine up to 15-h lifetimes, i.e., by reducing δ_{p0} to increase the signal, if no systematic effects are taken into account. For instance, it could be used to directly measure the magnetic-field-dependent linewidth of the Sr bosonic isotopes [51,78], determine the Sr $^3P_2$ excited-state lifetime or even longer-lived states such as the predicted ∼10-μHz nuclear transition on ^{229}Th being pursued as a next-generation clock [79–81], or obtain data on exotic systems of interest for atomic structure calculations, such as highly charged ions [52,82,83], in cases where suitable transitions can be found.

ACKNOWLEDGMENTS

We acknowledge helpful discussions with G. Greve, M. Norcia, and C. Sanner, as well as J. Ye and his group for providing narrow linewidth light from their clock laser. This work is supported by the NSF JILA-PFC PHY-1734006 grants, DARPA Extreme Sensing, and NIST. J.R.K.C. acknowledges financial support from NSF Graduate Research Fellowship.

APPENDIX A: LIGHT-MATTER INTERACTIONS

In this Appendix we explore the light-matter interactions and the phase shift acquired by a probe detuned from the atomic transition.

1. Optical Bloch equations

Following the conventions adopted in Ref. [66], we consider N two-level atoms, described by the usual Pauli operators $\hat{\sigma}_j^i$, with $i = x, y, z$ and $j = 1, \ldots, N$, equally coupled to a single-cavity mode with annihilation operator $\hat{c}$. In this case the Jaynes-Cummings Hamiltonian [62,63] in the atomic frame is

$$H = \hbar\delta_c \hat{c}^\dagger \hat{c} + \hbar g(\hat{c}\hat{J}^+ + \hat{c}^\dagger \hat{J}^-), \tag{A1}$$

where $\hat{J}^\pm = \sum_{i=1}^N \hat{\sigma}_i^\pm$ are the collective raising and lowering operators for the atoms, $\delta_c = \omega_c - \omega_a$ is the cavity detuning from the atomic transition (ω_a), and $2g$ is the single-photon Rabi frequency. We can further define $\hat{J}^z = \frac{1}{2}\sum_{i=1}^N \hat{\sigma}_j^z$, in order to have a closed angular momentum algebra.

If we add a cavity drive $c_i(t)$ at frequency ω_p, where c_i has units of $\sqrt{\text{photons/s}}$, we can use the input-output formalism [66,84] to write the Heisenberg-Langevin equations of motion for the cavity and atomic mean operators ($O = \langle \hat{O} \rangle$), on the atomic frame, as follows:

$$\begin{aligned} \dot{c} &= -\left(i\delta_c + \frac{\kappa}{2}\right)c - igJ^- + \sqrt{\kappa_m}c_i(t), \\ \dot{J}^- &= i2gJ^z c - \gamma_\perp J^-, \\ \dot{J}^z &= -ig(cJ^+ - c^* J^-) - \gamma\left(\frac{N}{2} + J^z\right), \end{aligned} \tag{A2}$$

where we have included the spontaneous emission rate γ, a transverse dephasing term $\gamma_\perp$, and cavity losses characterized by its linewidth κ. The single mirror transmission is characterized by $\sqrt{\kappa_m}$ ($\kappa = 2\kappa_m$). In the rotating frame, the incident cavity field is $c_i(t) = c_{i0}e^{-i\delta_p t}$, with $\delta_p = \omega_p - \omega_a$ the drive detuning from the optical transition.

2. Steady-state solution

In the presence of a driving field with detuning δ_p [$c_i(t) = c_{i0}e^{-i\delta_p t}$], the steady-state solution is characterized by observables of the form $J^- = \tilde{J}^- e^{-i\delta_p t}$ and $c = \tilde{c}e^{-i\delta_p t}$. Working in the weak probe approximation, such that all the atoms remain in the ground state, the transmitted field ($\tilde{c}_t = \sqrt{\kappa_m}\tilde{c}$) satisfies $\tilde{c}_t = T(\delta_p)c_{i0}$ for a transfer function $T(\delta_p)$ given by

$$T(\delta_p) = \frac{1}{1 - i\left(\frac{\delta_p - \delta_c}{\kappa/2}\right) + \frac{NC\gamma/2}{\gamma_\perp - i\delta_p}}, \tag{A3}$$

and for the collective atomic coherence $\tilde{J}^-$ is

$$\tilde{J}^- = \frac{igN\tilde{c}}{(i\delta_p - \gamma_\perp)}. \tag{A4}$$

Here we defined the cooperativity parameter as $C = (2g)^2/(\gamma\kappa)$.

The phase $\delta\varphi_t(\delta_p)$ acquired by the transmitted field [$\tilde{c}_t = |T(\delta_p)|e^{i\delta\varphi_t(\delta_p)}c_{i0}$] satisfies

$$\tan[\delta\varphi_t(\delta_p)] = \frac{-2\left[\delta_p g^2 N + (\delta_c - \delta_p)\left(\delta_p^2 + \gamma_\perp^2\right)\right]}{\gamma_\perp 2g^2 N + \kappa\left(\gamma_\perp^2 + \delta_p^2\right)}. \tag{A5}$$

Under the following hierarchy, realized in our system at the clock transition [17],

$$\begin{aligned} \sqrt{N}g &\sim \delta_p \ll \kappa, \\ \gamma_\perp &\ll \delta_p, \\ |\delta_c - \delta_p| &\sim \delta_p, \end{aligned} \tag{A6}$$

we can approximate

$$\tan[\delta\varphi_t(\delta_p)] \approx -\frac{2g^2 N}{\kappa\delta_p} - \frac{2(\delta_c - \delta_p)}{\kappa}, \tag{A7}$$

which can be rewritten as

$$\tan[\delta\varphi_t(\delta_p)] \approx -\frac{NC\gamma}{2\delta_p} - \frac{2(\delta_c - \delta_p)}{\kappa}. \tag{A8}$$

The first term on the right-hand side of Eq. (A8) is the atomiclike phase shift, while the other term is a cavitylike phase shift, independent of the atoms. For our measurements, we are interested in the first term as it encodes the collective interactions (Ng^2), while the last term can be measured independently and subtracted, by for example measuring the phase shift of an identical tone one free spectral range away. For our system, the atomiclike phase shift [$NC\gamma/(2\delta_p)$] is typically 30 mrad, while the on-resonance cavitylike phase shift ($2\delta_p/\kappa$) is typically 15 mrad, for $\delta_p/(2\pi) = 1$ kHz.

As described in the main text, we take the difference between the pairwise phases on two consecutive cavity modes. A detailed description is given in the next section. The total

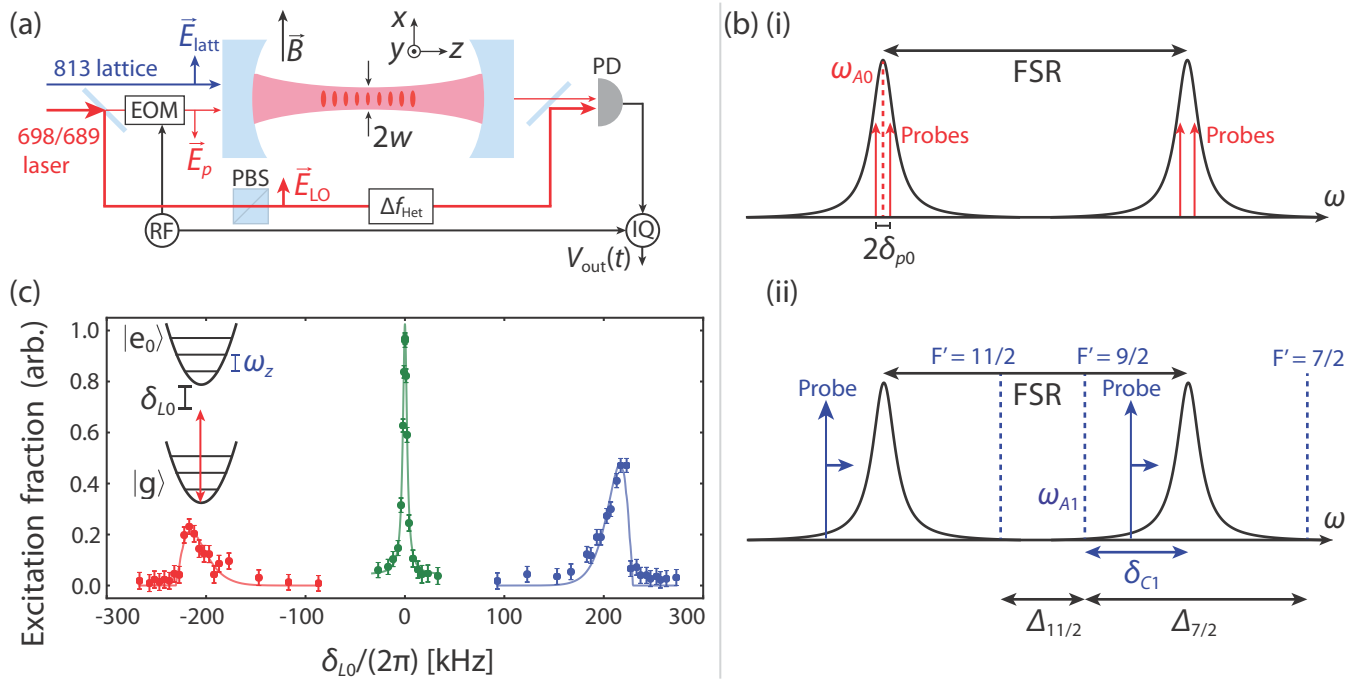

FIG. 4. (a) Experimental setup. An 813-nm optical lattice confines atoms at 14(1) μK. A 689- and 698-nm laser addresses the atomic transitions between the ground $^1S_0$ state and the $^3P_1$ and $^3P_0$ states, respectively. The different frequency tones to generate the probes, as described in the main text, are generated by an in-fiber EOM and rf function generators operating at the different necessary frequencies. Most of the light constitutes an optical local oscillator. The local oscillator is frequency shifted by $\Delta f_{\rm Het}$, polarization filtered along $\hat{x}$ with a polarization beam splitter, and is beat with the transmitted probes into a photodiode. The photocurrent is properly demodulated by each rf frequency and recorded as a different voltage $V_{\rm out}(t)$. (b) The probe tones used to address the clock transition are shown in (i), while the tones and hyperfine levels for the excited $^3P_1$ manifold are shown in (ii). The detuning δ_{C1} is defined with respect to the $F = \frac{9}{2}$ manifold. Frequencies not to scale. (c) Vibrational spectroscopy on the clock transition. We scan the detuning δ_{L0} of a strong 698-nm probe and record the excitation fraction. We follow the procedure in Ref. [65] to fit the occupation number, temperature, and trap frequency.

phase shift, defined as $\Delta\varphi_0$ in the main text, becomes

$$\Delta\varphi_0 = -\frac{NC\gamma}{\delta_p}\left(1 - 4\frac{\delta_c^2}{\kappa^2} + 4\frac{\delta_p^2}{\kappa^2} + \frac{(NC\gamma)^2}{12\delta_p^2} - \frac{NC\gamma}{\kappa}\right). \quad \text{(A9)}$$

Higher-order terms in Eq. (A9) show higher-order corrections on the phase shift, that will be considered as corrections (see systematic section later).

Finally, we want to note that at short times, there is an initial transient ringing, of duration $NC\gamma$, associated with the homogeneous solution of the optical Bloch equations, that in our system lasts about 2 ms.

3. Excitation fraction

If we break the weak probe power approximation, and allow the inversion to change during the probing, using Eqs. (A2) and (A4) we find that the steady-state excitation fraction is

$$N_e/N \approx \frac{\gamma_\perp C}{\delta_p^2 + \gamma_\perp^2}|c_{i0}|^2, \quad \text{(A10)}$$

showing the characteristic $1/\delta_p^2$ dependence of these dispersive measurements.

In the absence of dephasing ($\gamma_\perp = \gamma/2$), the steady state is reached on a $1/\gamma$ timescale. Therefore, for a measurement window T_m, the fraction of atoms in the excited state at the end of the measurement will be

$$(N_e/N)_{T_m} \approx \gamma T_m \frac{\gamma C}{2\delta_p^2}|c_{i0}|^2. \quad \text{(A11)}$$

We will adjust the power, i.e., $|c_{i0}|^2$, such that $(N_e/N)_{T_m} \ll 1$ over the measurement window. Ideally, this constraint, and the final quantum efficiency, will limit the resolution of the atom counting as a nondestructive process.

Furthermore, this suggests that even if the inversion is changing because of a different process rather than the excitation caused by the tones, the atomiclike phase shift $\Delta\varphi_0$ can be used to dynamically track the atomic inversion $J_z(t)$ [85].

APPENDIX B: EXPERIMENTAL SETUP

A detailed scheme of the experimental setup is given in Fig. 4(a) and it has been already detailed in Refs. [23,24,35]. Atoms are loaded into a 813-nm near-magic wavelength intracavity optical lattice, following cooling and trapping on the 7.5-kHz transition ($^1S_0 \rightarrow {}^3P_1$) at 689 nm [86]. The lattice is near magical for the $^1S_0 \rightarrow {}^3P_0$ millihertz clock transition at 698 nm, with a detuning of maximally ~2 GHz from the magic wavelength (half free spectral range). As in the main text, from here on all the 0(1) subindices refer to quantities defined on the $^1S_0 \rightarrow {}^3P_0$ ($^3P_1$) transition.

For both the clock and the 7.5-kHz transitions, a small fraction of the light is coupled into the same in-fiber electro-optical phase modulator (EOM) and sent to the optical resonator. Which light enters the modulator at a given time is controlled by acousto-optic modulators prior to the phase modulator. Both probes are polarized along the quantization direction $\hat{z}$, established by a static magnetic field $\vec{B}$. The different probe tones are driven by different radio-frequency (rf) sources, indicated by a generic rf generator in Fig. 4(a). The different cavity modes probed for each transition are shown in Fig. 4(b), which also indicates the relative frequency difference of the hyperfine states of the $^3P_1$ excited state. Further details for the individual transitions are provided below.

1. Probing $^3P_0$

The clock transition $^3P_0$ is probed with two tones nominally detuned by $\pm\delta_p = \pm 1$ kHz from atomic resonance [see Fig. 4(b)(i)]. An identical pair of probe tones offset by one free spectral range ($\Delta_{\mathrm{FSR},0}$) probes the phase shifts induced by the empty cavity resonance. Since this second pair of probe tones is far from resonance, we can use much more power in these probe tones to reduce their photon shot-noise contributions to the final signal to noise.

The probe tones are typically applied for 20 to 40 ms. We remove the first interval of width $\mathrm{T_H} \approx 5$ ms, where the initial transient is large. Using two probe tones near the atomic transition provides first-order insensitivity to laser frequency uncertainty and noise relative to the atomic transition frequency. Using the full four-tone probe technique provides cavity and laser frequency noise rejection, as well as automatic rejection of the empty cavity phase shift.

A large fraction of the laser light is picked off prior to the phase modulator and frequency shifted by Δf_{LO} to provide a local oscillator $\vec{E}_{\mathrm{LO}}$, linearly polarized along $\hat{x}$. The LO is frequency shifted by $\Delta f_{\mathrm{LO}} = 20$ kHz, polarization filtered by a polarization beam splitter that transmits light polarized along $\hat{x}$, and combined with the transmitted tones onto a fast photodetector (PD), forming a heterodyne beat note [Fig. 4(a)] with photon shot-noise limited sensitivity.

After amplification, both pairs of probe tones are separately in-phase and quadrature (IQ) demodulated to a base band of 20 kHz using the same RF sources used to drive the phase modulator. The demodulated IQ voltage signals $V_{\mathrm{IQ}}(t)$ are digitally sampled into the computer and then fitted to extract the difference in the phases for a single pair. For example, the near-resonant pair of tones that probe the clock transition are demodulated to 20 ± 1 kHz, for $\delta_{p0}/(2\pi) = 1$ kHz.

After computing the four individual phases $\delta\varphi_0(\pm\delta_p)$ and $\delta\varphi_0(\Delta_{\mathrm{FSR},0} \pm \delta_p)$, we compute the appropriate pairwise differences to arrive at an estimate of the atomic phase shift $\Delta\varphi_0 = [\delta\varphi_0(\delta_p) - \delta\varphi_0(-\delta_p)] - [\delta\varphi_0(\Delta_{\mathrm{FSR},0} + \delta_p) - \delta\varphi_0(\Delta_{\mathrm{FSR},0} - \delta_p)]$ that for the small angles here is related to the atomic linewidth γ_0 by $\Delta\varphi_0 = -NC_0\gamma_0/\delta_{p0}$.

2. Probing $^3P_1$

The 7.5-kHz transition $^1S_0$ to $^3P_1$ is probed using a total of two tones separated by one free spectral range [see Fig. 4(b)(ii)]. Both tones are linearly swept in frequency at the same time, and as described above, the transmitted probe light is heterodyne detected, amplified, the individual probe tones are IQ demodulated, and digitally sampled into the computer. The IQ data are fitted to extract the resonance frequency $\delta\omega_1$ of each cavity mode up to a common offset, and an estimate of the differential frequency shift between the two cavity modes $\Delta\omega_1$ is then computed.

3. Axial sideband spectroscopy

We determine the mean occupation number, trap frequency, and temperature via axial sideband spectroscopy using a cavity probe near resonance with the clock transition, following the approach of Ref. [65]. The fraction of atoms excited by this probe as we scan its frequency is shown in Fig. 4(c). We consistently measure the axial trap frequency to be $\omega_z/(2\pi) = 230(1)$ kHz, the temperature to be $T = 14(1)\ \mu$K, and the mean occupation number $\bar{n}_z = 0.9(1)$. The Lamb-Dicke parameter computed for the $^3P_0$ transition is $\eta_0 = 0.1425(6)$ and $\eta_1 = 0.1443(6)$ for the $^3P_1$ transition. Remarkably, the measurement is dispersive ($\delta_{p0} \gg NC_0\gamma_0$), but addresses the carrier transition ($\delta_{p0} \ll \omega_z$), which is achievable for this set of ultranarrow optical transitions.

4. Cavity geometry determination

In order to set the detuning of the cavity to the $F = \frac{9}{2}$ $^3P_1$ manifold (δ_{C1}), while keeping the cavity on resonance with the clock transition, we heat up our ceramic cavity spacer with a set of lights by about 10 K from room temperature. At these settings, we measure a free spectral range (FSR) of $\Delta_{\mathrm{FSR},0} = 2\pi \times 3.714\,61(3)$ GHz for the clock transition and $\Delta_{\mathrm{FSR},1} = 2\pi \times 3.714\,59(2)$ GHz for the 7.5-kHz transition. The cavity waist at the clock transition $^3P_0$ wavelength is determined to be $\mathrm{w}_0 = 73.85(7)\ \mu$m. For the broader transition $^3P_1$ transition's wavelength, the waist is $\mathrm{w}_1 = 73.37(7)\ \mu$m. These values are predicted by the Gaussian beam propagation theory using the known wavelengths, mirror radius of curvature, and cavity free spectral range. The waist sizes have been independently verified to agree at the 0.1% level by measuring the spacing between the TEM_{00} mode and the $\mathrm{TEM}_{1,0/0,1}$ modes relative to the measured free spectral range of the cavity [74].

Atoms are loaded at the cavity center (in-between the two mirrors), as confirmed by taking fluorescence images of the loaded atoms. The Rayleigh length of the modes [$\sim$2.453(5) cm] is typically much longer than the longitudinal extent of the cold atomic cloud [$\sigma_{\mathrm{long}} = 0.30(5)$ mm]. Finally, we performed cavity ring-down measurements to determine the cavity linewidth. For these measurements we probed the cavity on resonance with light polarized along $\hat{x}$ and after quickly turning off the probe light with the electro-optical modulator (EOM), we observed the photocurrent on a fast dc coupled photodiode directly positioned after the cavity. We determine a linewidth of $\kappa_0/(2\pi) = 140.9(3)$ kHz at the clock transition and $\kappa_1/(2\pi) = 153.0(4)$ kHz at the 689-nm transition, after taking statistics over several trials. The cavity and atomic parameters can be found in Table II.

TABLE II. Summary of cavity and atomic parameters.

Description	Symbol	Value	Unit
Probe wavelength 0: $^3P_0$ probe [87]	λ_0	698.4457	nm
Probe wavelength 1: $^3P_1$ probe [87]	λ_1	689.4485	nm
Trap wavelength	$\lambda_{\rm trap}$	813.4257(2)	nm
Cavity FWHM 0 for probe polarized along $\hat{x}$	$\kappa_0/2\pi$	140.9(3)	kHz
Cavity FWHM 1 for probe polarized along $\hat{x}$	$\kappa_1/2\pi$	153.0(4)	kHz
Mode waist 0	w_0	73.85(7)	μm
Mode waist 1	w_1	73.37(7)	μm
Lattice waist	$\mathrm{w}_{\rm trap}$	79.7(1)	μm
Rayleigh range 0,1	z_R	2.453(5)	cm
Free spectral range 0	$\Delta_{\rm FSR,0}/2\pi$	3.71461(3)	GHz
Free spectral range 1	$\Delta_{\rm FSR,1}/2\pi$	3.71459(2)	GHz
Cavity length 0	L_0	4.03532(3)	cm
Cavity length 1	L_1	4.03534(2)	cm
Axial trap frequency on axis	$\omega_z/2\pi$	230(1)	kHz
Radial trap frequency	$\omega_r/2\pi$	528(2)	Hz
Axial temperature	T_z	14(1)	μK
Radial temperature	T_r	12(2)	μK
rms thermal radius	σ_r	14(1)	μm
rms longitudinal cloud radius	$\sigma_{\rm long}$	0.30(5)	mm
Axial vibrational quanta	$\bar{n}_z$	0.9(1)	
Axial Lamb-Dicke parameter 0	η_0	0.1425(6)	
Axial Lamb-Dicke parameter 1	η_1	0.1443(6)	
Cavity detuning 0	$\delta_{C0}/2\pi$	0(10)	kHz
Cavity detuning 1	$\delta_{C1}/2\pi$	277.5(8)	MHz
Birefringent cavity mode full splitting 0	$\delta_{b0}/2\pi$	23(3)	kHz
Birefringent cavity mode full splitting 1	$\delta_{b1}/2\pi$	24(3)	kHz
Birefringent cavity mode polar angle on Poincaré sphere (Jones vector)	θ_b	30(2)	deg
Birefringent cavity mode azimuthal angle on Poincaré sphere (Jones vector)	φ_b	$\pm$14(4)	deg
$^3P_1$ linewidth [75]	$\gamma_1/2\pi$	7.48(1)	kHz
$^3P_1$ $F' = 11/2$ detuning from 9/2 [87]	$\Delta_{11/2}/2\pi$	$-$1463.15(6)	MHz
$^3P_1$ $F' = 7/2$ detuning from 9/2 [87]	$\Delta_{7/2}/2\pi$	1130.26(6)	MHz

APPENDIX C: EXTRACTING $(g_0/g_1)^2$ FROM MEASURED PHASE SHIFTS

We measure the ratio $(g_0/g_1)^2$ by interleaved measurements of the atomic-induced phase shift between two probes near resonant with the clock transition $\Delta\varphi_0$ and cavity frequency shift $\Delta\omega_1$ on the 7.5-kHz transition, from which we calculate the associated phase shift $\Delta\varphi_1 = \Delta\omega_1/(\kappa_1/2)$. An ideal measurement assumes that all the atoms are homogeneously coupled to the cavity mode, they do not move, they are optically pumped to the $m_F = \pm\frac{9}{2}$ states, all the atoms remain in the ground state during the probing, both probes are π polarized, and that the cavity mode is aligned to the clock transition, while the 689 $F = \frac{9}{2} \rightarrow F' = \frac{9}{2}$ transition is detuned by δ_{C1}. The validity of these approximations will be taken into consideration when analyzing the systematic corrections.

The atomic contribution to the phase shift on the clock transition between tones at $\pm\delta_{p0}$ with respect to the atomic transition is

$$\Delta\varphi_0 = \frac{4Nc_C^2 g_0^2}{\kappa_0 \delta_{p0}}, \tag{C1}$$

where c_C is the Clebsch-Gordan coefficient for π-polarized light probing the stretched states ($c_C = \sqrt{\frac{9}{11}}$), $2g_0$ is the single-photon Rabi frequency for the clock transition, and κ_0 is the cavity linewidth at 698 nm.

The difference between the cavity frequency shifts for the two 689-nm modes, as shown in Fig. 4(b)(ii), is

$$\Delta\omega_1 = Ng_1^2\left\{\left(\frac{c_{N1}^2}{\delta_{C1}} + \frac{c_{N2}^2}{\delta_{C1} - \Delta_{11/2}}\right) - \left(\frac{c_{N1}^2}{\delta_{C1} - \Delta_{\rm FSR,1}} + \frac{c_{N2}^2}{\delta_{C1} - \Delta_{11/2} - \Delta_{\rm FSR,1}}\right)\right\}, \tag{C2}$$

where c_{N1} and c_{N2} are the Clebsch-Gordan coefficient for π-polarized light probing the stretched states on the $F = \frac{9}{2} \rightarrow F' = \frac{9}{2}$ and $F = \frac{9}{2} \rightarrow F' = \frac{11}{2}$ transitions, respectively ($c_{N1} = \sqrt{\frac{9}{11}}$, $c_{N2} = \sqrt{\frac{2}{11}}$), $\Delta_{11/2}/(2\pi) = -1463.15(6)$ MHz is detuning of $F' = \frac{11}{2}$ with respect to the $F' = \frac{9}{2}$

TABLE III. Correction factors F_C for $\Delta\varphi_1$ measurement.

Effect	$1 - F_C$	Uncertainty on F_C
Polarization uncertainty	2×10^{-4}	6×10^{-5}
Differential lattice shift	-2.3×10^{-3}	8×10^{-4}
Saturation during probe	-2×10^{-4}	2×10^{-4}
Probe optical pumping and losses	-4×10^{-4}	4×10^{-4}
Zeeman shift	2×10^{-8}	1×10^{-9}
Higher-order corrections	-2.5×10^{-4}	1×10^{-4}

manifold [87], and $\Delta_{\mathrm{FSR},1}/(2\pi)$ is the cavity free spectral range at 689 nm. Note that the $F' = \frac{7}{2}$ manifold, detuned by $\Delta_{7/2}/(2\pi) = 1130.260(6)$ MHz from the $F' = \frac{9}{2}$ transition, does not contribute to the expression in Eq. (C2) as we are assuming atoms are optically pumped to $m_F = \pm\frac{9}{2}$ and the probe is π polarized.

To finally reveal the ratio between g_0 and g_1, we need to precisely know all the numerical factors in Eqs. (C1) and (C2), as well as characterize all systematic corrections that must be applied to account for deviations of the experiment from the idealized situation above.

APPENDIX D: SYSTEMATIC EFFECTS

This measurement approach for determining natural lifetimes of long-lived states is unique, and it is important to think broadly about potential systematic corrections that must be applied, as well as the uncertainties on these corrections. In this Appendix, we will discuss nearly 20 different systematic corrections. Most of these are small enough to be ignored, but we include them for completeness and for the sake of future applications of the technique, in which details of the experimental system might make these effects larger.

We roughly break up the systematics discussion into three categories: those that affect individually the cavity phase shift measurement $\Delta\varphi_1$ on the 7.5-kHz transition, those that affect the phase shift measurement $\Delta\varphi_0$ on the clock transition, and those that affect the measured ratio $(\Delta\varphi_0/\Delta\varphi_1)$. We define the correction factors F_C as the ratio of the ideal quantity Q^i and the actually measured quantity Q^m such that the ideal quantity can be recovered from the measured quantity as $Q^i = F_C Q^m$.

1. Corrections on the phase shift $\Delta\varphi_1$

In this section we discuss effects that affect the measured cavity frequency shift $\Delta\varphi_1$ for the two consecutive TEM_{00} modes on the 7.5-kHz transition at 689 nm. The magnitude of the correction factors F_C are shown in Table III.

a. Polarization uncertainty in $^3P_1$ probe

The polarization uncertainty effect refers to the fact that the probe light's polarization might not have been perfectly π polarized. To optimize the probe polarization's orientation relative to the magnetic field, we performed a measurement of $\Delta\varphi_1$ at a (variable) value of the transverse magnetic field B_t first, and within 4 ms we measure it again at another magnetic field B_t^{ref} that we believe to be close to the value that cancels the transverse components. Magnetic fields along $\hat{x}, \hat{y}, \hat{z}$ are generated by three respective sets of Helmholtz coils driven by a stabilized current source, which allow us to rapidly perform small changes in the y and z components of B_t in order to perform this measurement [see Fig. 4(a)]. In this way, we have the ability to compute the ratio in each experimental repetition, which gives us further insensitivity with respect to other quantities that fluctuate shot to shot, like atom number.

The ratio of the two measurements $\Delta\varphi_1(B_t)/\Delta\varphi_1(B_t^{\mathrm{ref}})$ is maximized when the y and z components are nulled, as our model shows. An example of this measurement is shown in Fig. 5(a). If the reference field B_t^{ref} was not properly chosen, we can change it accordingly and evaluate the ratio again, until we consistently find the right value for B_t^{ref}, where we would like to operate the experiment. Typically, we observed day-to-day shifts of 3 mG as we repeat this procedure before any of the measurements to establish the linewidth ratio. The associated correction factor F_C takes into account the effect of a small magnetic field fluctuations of magnitude 3 mG on typical data sets as shown in Fig. 5(a). Based on our model, we find that we can realize a probe with 98% pure π polarization. The fitted quadratic dependence of the phase shift magnitude along with this 3-mG uncertainty is used to estimate the correction factor for this effect.

b. Differential lattice shift in $^3P_1$ probe

The differential lattice shift is due to the fact that the lattice is not quite magic for the $^3P_1$ states. However, the expected differential ac Stark shifts, around 0.7(2) MHz for our trap depth, are very small compared to the cavity detuning from the atomic transition δ_{C1}. Experimentally, we determine $\Delta\varphi_1$ to change by less than 1% for trap depths changing by 50%. The uncertainty is estimated based on a combination of trap depth, resonance frequency, and cavity detuning uncertainties.

c. Saturation and optical pumping due to the $^3P_1$ probe

While probing the cavity phase shift $\Delta\varphi_1$, the probe itself can excite atoms, especially if the probe power is large. To characterize this effect, we measure the change in $\Delta\varphi_1$ as a function of the probe power. In each experimental repetition, we perform three consecutive measurements as depicted in Fig. 5(b): first at a (variable) power P_1^H, then at a (low) reference power P_1^L, then again at the same (variable) power P_1^H. This allow us to be insensitive to, for instance, shot-to-shot variations in atom number, while allowing us to characterize the effect of a high-power probe on each measurement.

In each experimental shot, we obtain three cavity phase shifts for each of the previous powers that we denote as $\Delta\varphi_1^1$, $\Delta\varphi_1^2$, and $\Delta\varphi_1^3$, respectively. We model the effect of any possible probe power related effect during the probe, in the low-power limit, as a modification in the measured phase shift as $\Delta\varphi_1(P) = \Delta\varphi_1(P=0)[1 - 2(P/P_0)]$, where P is the probe optical power, P_0 is some parameter that works as an effective saturation power in this model (the beam area is fixed by the cavity), and $\Delta\varphi_1(P=0)$ is the zero-power phase shift that is the interest of our measurement. In order to characterize this behavior, we change P_1^H and measured the effect on $\Delta\varphi_1$ using the ratio $s_S = [(\Delta\varphi_1^1 + \Delta\varphi_1^3)/2 - \Delta\varphi_1^2]/(\Delta\varphi_1^2)$; for low excitation fractions, this is linear in the input power P_1^H

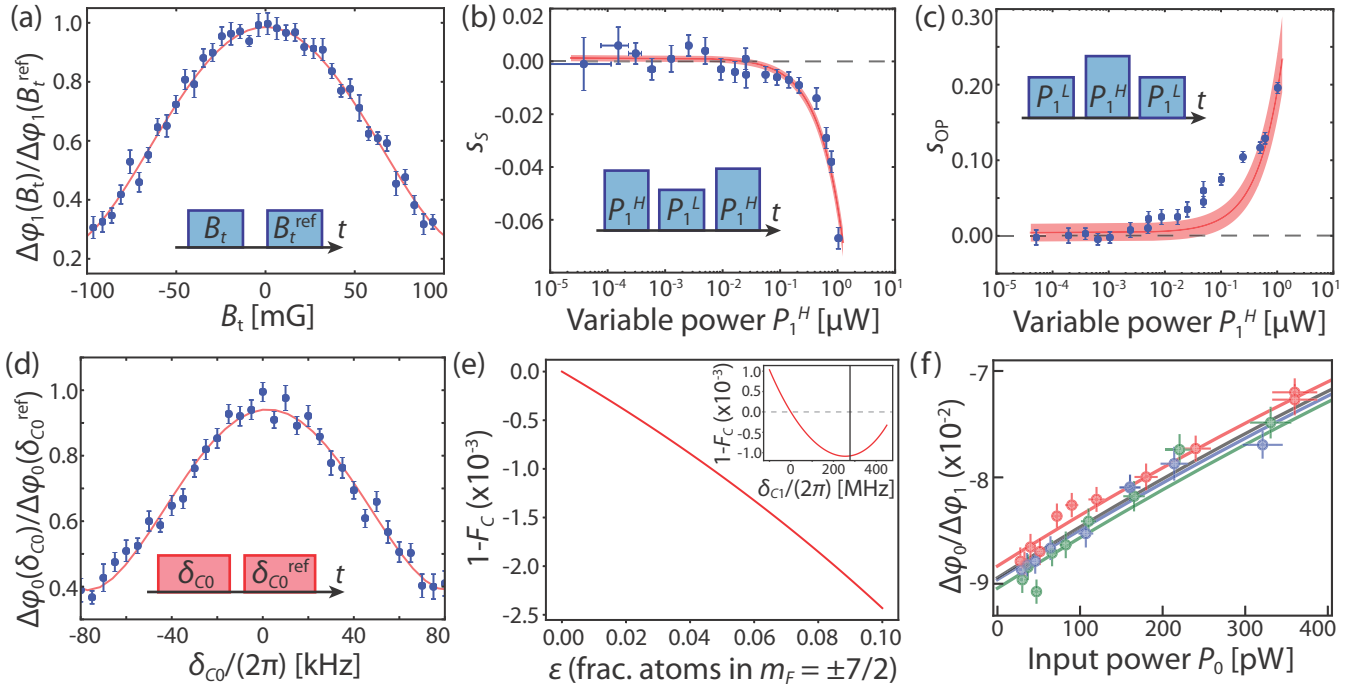

FIG. 5. (a) Polarization alignment using cavity phase shift measurements while changing one of the transverse magnetic field components. In a single shot, we compute the ratio between two measurements at a variable transverse field B_t and a reference transverse field $B_t^{\rm ref}$. Typical day-to-day fluctuations are around 3 mG. (b) Saturation effects on the 689-nm transition probe. We use interleave $\Delta\varphi_1$ measurements at different powers to determine the relative reduction on $\Delta\varphi_1$ as the probe power increases. (c) Power-induced reduction on the 689-nm transition phase shift. We use interleave $\Delta\varphi_1$ measurements at different powers to determine the relative reduction on $\Delta\varphi_1$ as the probe power increases. (d) Influence of the cavity detuning δ_{C0} on the atomlike phase shift $\Delta\varphi_0$ on the clock transition. We tune the cavity at two different cavity detunings, one fixed $\delta_{C0,\rm ref}$, and one variable δ_{C0}, and in a single show we compute the ratio $\Delta\varphi_0(\delta_{C0})/\Delta\varphi_0(\delta_{C0,\rm ref})$ that maximizes when $\delta_{C0} = \delta_{C0,\rm ref} = 0$. (e) Optical pumping correction factor F_C, where we take the fractional population on the $\pm\frac{7}{2}$ states to be ε, on the $\pm\frac{5}{2}$ states is ε^2, on the $\pm\frac{3}{2}$ states is ε^3, and on the $\pm\frac{1}{2}$ states is ε^4. Inset shows the dependence of the correction factor for $\varepsilon = 0.05$ versus the cavity detuning δ_{C1} to the $^3P_1$, $F' = \frac{9}{2}$ manifold. (f) Zoom-in for low powers for Fig. 3(c) in the main text. Results and fits shown for estimator E_3 as described in this text.

and scales as $s_S = (P_0 - 2P_1^H)/(P_0 - 2P_1^L)$. For a given probe power P, the correction factor would be $F_C = 1/[1 - 2(P/P_0)]$. As we measure P_1^L and s_S, we can determine P_0 in our model to estimate the correction.

The measurement is shown in Fig. 5(b), where we fit a linear function (red line) to the input probe power P_1^H. This allows us to establish that the excitation fraction is not significant (<0.0001) for cavity probe input powers below 1 nW. The value quoted for the associated correction factor takes into account the maximum power used for the data presented in Fig. 3(b) in the main text, which was around 1 nW and was decreased together with the clock transition probe power to extract the ratio $\Delta\varphi_0/\Delta\varphi_1$. The uncertainty is taken to cover the full range of power used in the $\Delta\varphi_0/\Delta\varphi_1$ measurement presented in the main text. We assign a value $F_C = 1.0002(2)$ for the correction factor.

Furthermore, the probe itself can cause more permanent effects. For instance, it can cause atom loss or optically pump atoms to different magnetic sublevels, modifying $\Delta\varphi_1$ and eventually $\Delta\varphi_0$ on interleaved measurement sequences. To characterize this effect, we again use three consecutive measurements to obtain $\Delta\varphi_1^1$, $\Delta\varphi_1^2$, and $\Delta\varphi_1^3$: first at a (low) reference power P_1^L, then at a (variable) power P_1^H, then again at a (low) reference power P_1^L. This scheme allow us, in a single shot, to characterize the change that occurs after applying a relative high-power probe.

The values for P_1^L used here fall into the low-power region from the the previous analysis, such that for simplicity we will consider they do not have a significant effect. However, we will consider the second high-power probe has a more permanent effect. For example, we consider the case that during, and after, the second pulse with power P_1^H the measured phase shift is modified by an effective value $[1 - (P_1^H/P_{OP})]$ from its zero-power value. Again, this P_{OP} tries to capture any effect such as redistribution in the ground-state hyperfine state manifold or atom loss as consequence of a higher probe power.

To characterize this effect and estimate the necessary correction, we consider the parameter $s_{OP} = 1 - (\Delta\varphi_1^3)/(\Delta\varphi_1^1)$, that measures the differential phase shift after applying a higher probe power in-between the two pulses. In particular, our model predicts a behavior of the form $s_{OP} = (P_1^H/P_{OP})$. We show the result of these measurements in Fig. 5(c), where we varied the optical power of the second probe P_1^H. For the final optical power used in the phase shifts ratio measurement presented in the text, we use maximum probe powers in the 689-nm transition on the order of 1 nW. From this characterization, we assign a correction factor $F_C = 1.0004(4)$ to cover the full range of variation for the used powers.

TABLE IV. Correction factors F_C for $\Delta\varphi_0$ measurement.

Effect	$1-F_C$	Uncertainty on F_C
Polarization uncertainty	-3×10^{-4}	3×10^{-4}
Atomic resonance uncertainty	6×10^{-3}	6×10^{-3}
Cavity resonance drift	-8×10^{-3}	6×10^{-3}
Zeeman shift	2.3×10^{-3}	5×10^{-4}
Higher-order corrections	4×10^{-4}	2×10^{-4}

d. Zeeman shifts in $^3P_1$ probe

The Zeeman shift on the different ground and excited states changes the effective atom-cavity detuning by a few hundred kHz, which is much smaller than the cavity detuning δ_{C1}. The typical magnetic field that we use is 95 mG, as calibrated using the splitting between the peaks in the superradiant pulses [24] and corroborated by the splitting measured in Fig. 2(a) in the main text, for example. Taking this effect into account, we expect a very small correction to the ratio of phase shifts.

e. Higher-order corrections on $\Delta\varphi_1$ measurement

Higher-order corrections on the cavity frequency shift manifest in $\delta\omega_1$ as $\delta\omega_1 = Ng_1^2/\delta_{C1}(1-2Ng_1^2/\delta_{C1}^2)$ [66]. We note that this correction is N dependent. For typical experimental parameters we have $2Ng_1^2/\delta_{C1}^2 \lesssim 1\times10^{-3}$. We calculate the correction factor F_C based on an independent atom-number calibration using florescence imaging, while its uncertainty is estimated assuming extreme 50% fluctuations in typical N.

2. Corrections on the phase shift $\Delta\varphi_0$

In this section we discuss effects that affect the measured atomiclike phase shift $\Delta\varphi_0$ on the millihertz transition at 698 nm. The magnitude of the correction factors F_C are shown in Table IV.

a. Polarization uncertainty in $^3P_0$ probe

The polarization uncertainty correction takes into account any possible misalignment between the probe polarization and the applied magnetic field that defines the quantization axis. Based on the measurements for $\Delta\omega_1$ presented before, we model in a very similar way what the effect would have been for the atomic phase measurement $\Delta\varphi_0$ with a typical 3-mG uncertainty on the transverse magnetic fields.

b. Atomic resonance uncertainty in $^3P_0$ probe

The clock transition is addressed with light from a state-of-the-art laser, used in the ^{87}Sr optical lattice clock experiments at JILA [2,3,60]. To determine the atomic resonance, we perform Rabi spectroscopy, measuring the excitation fraction versus the probe light's frequency. The probe frequency is changed by changing the in-fiber EOM driving frequency. For sufficiently low power, we are able to determine the central frequency with less than 10 Hz uncertainty, but the full width at half-maximum of the spectroscopic feature is typically between 50 and 100 Hz, similar to the data shown in Fig. 2(b) in the main text. The frequency might be shifted from the natural ^{87}Sr frequency due to various atomic frequency shifts, such as dc Stark shifts, Doppler shifts, collective shifts, and differential ac Stark shifts from a lattice imperfectly tuned to the clock state's magic wavelength. However, we have already fully characterized all these possible clock transition frequency shifts to be well below 100 Hz in Ref. [24].

Because we are using two symmetric tones to address the atomic transition, the associated correction factor F_C to the measured phase shift scales as $[1-(\delta_{L0}/\delta_{p0})^2]$ with δ_{L0} the detuning from the tones central frequency to the atomic transition, as defined in the main text. Note that this effect increases the absolute value of the measured phase shift $\Delta\varphi_0$, as can be seen in Fig. 2(b) in the main text. Assuming that $|\delta_{L0}|/(2\pi) < 100$ Hz but is equally likely to take on any value in this range, we calculate a correction factor centered on the root-mean-square (rms) average of $F_C(\delta_{L0})$ over possible values of δ_{L0}, accompanied by an uncertainty large enough to cover the full range.

c. Cavity resonance uncertainty in $^3P_0$ probe

By probing and subtracting the phase shifts for two consecutive TEM_{00} modes, one on resonance with the atomic clock transition, we guarantee that any instantaneous cavity length fluctuation will be instantaneously removed from our measurement. However, if the initial cavity detuning from the clock transition δ_{C0} is nonzero, the phase shift will be modified by a factor $[1+(\delta_{C0}/(\kappa_0/2))^2]$, as noted in Eq. (A9). Typically, we can align the initial cavity length and minimize cavity drifts such that $|\delta_{C0}|/(2\pi) \leqslant 10$ kHz during each of the measurement in Fig. 3(b) in the main text. We had verified analytically and experimentally what would be the effect of a cavity resonance drift, with good agreement. For example, Fig. 5(d) shows the relative change in $\Delta\varphi_0$ as δ_{C0} is intentionally changed. For this measurement, we are able to change the cavity detuning by changing the drive voltage on the PZTs after the atoms are already loaded in the lattice, as shown in the inset. We first measure $\Delta\varphi_0$ for a variable detuning δ_{C0} and then change the cavity length to a reference detuning $\delta_{C0}^{\mathrm{ref}}$, which allow us to remove unwanted effects, such as atom-number drifts, from our measurements as we did when we analyze the impact of transverse components of the magnetic field on the phase measurements. Based on these results, and a precise determination of the cavity FSR, we estimate a correction of less than 1% if we average over cavity detunings below a maximum 10-kHz drift. In fact, the drifts in the zero-power value for $\Delta\varphi_0/\Delta\varphi_1$ reported in Fig. 3(b) in the main text are consistent with cavity frequency misalignment within our 10-kHz uncertainty.

d. Zeeman shift in $^3P_0$ probe

The small magnetic field present to define the quantization axis generates a Zeeman splitting between the two ground states, of typical magnitude 100 Hz, smaller than the probes splitting $2\delta_{p0}/(2\pi) = 2$ kHz. We can accurately calibrate the magnetic field by observing the splitting between superradiant pulses, as in Ref. [24]. By using two symmetric tones to address the clock transition, the phase shift will be only second-order sensitive to the Zeeman splitting. We calculate

TABLE V. This table contains the correction factors F_C to correct the ratio $(\Delta\varphi_0/\Delta\varphi_1)$.

Effect	$1-F_C$	Uncertainty on F_C
Offsets in $\Delta\phi_{0,1}$	0	1×10^{-2}
Axial inhomogeneous		
Probe coupling	0	2×10^{-3}
Differential radial average	7×10^{-5}	1×10^{-5}
Finite axial confinement/ resolved carrier correction	-6.2×10^{-2}	4×10^{-3}
Ground-state m_F distribution	-1×10^{-3}	1×10^{-3}
Lifetime in the lattice	-2×10^{-3}	2×10^{-3}
Cavity birefringence	-1.2×10^{-2}	5×10^{-3}

this value and assign an uncertainty based on a 5% uncertainty on the determination of the magnetic field along the quantization axis.

e. Higher-order corrections on the $\Delta\varphi_0$ measurement

Higher-order corrections on the four-tones phase shift method are derived in Eq. (A9). The second correction factor $[(2\delta_c/\kappa)^2]$ is the cavity resonance drift considered above. The other higher-order terms, remnant from the small-angle approximation, contribute at the level of 10^{-4} for typical atom numbers, obtained through an independent calibration of our fluorescence imaging. Its uncertainty is estimated assuming extreme 50% fluctuations in typical N.

3. Corrections on the ratio $(\Delta\varphi_0/\Delta\varphi_1)$

In this section we discuss effects that modify both the measured atomiclike phase shift $\Delta\varphi_0$ on the millihertz transition at 698 nm and the cavity phase shift $\Delta\varphi_1$ on the 7.5-kHz transition at 689 nm. The magnitude of the correction factors F_C is shown in Table V.

a. Offsets in $\Delta\varphi_{0,1}$

The effect of noncanceled offsets in our measurements is to alter the measured values of $\Delta\varphi_0$ and $\Delta\varphi_1$. In particular, because the desired phase shifts are collective, while the offset are not, it can cause an N-dependent correction to the ratio $\Delta\varphi_0/\Delta\varphi_1$.

Assuming single-atom phase shifts $\Delta\varphi^a_{0,1}$ and offsets $\Delta\varphi^{\rm off}_{0,1}$ on each measurement, we can express the desired ratio as

$$\frac{\Delta\varphi_0}{\Delta\varphi_1}=\frac{N\Delta\varphi^a_0+\Delta\varphi^{\rm off}_0}{N\Delta\varphi^a_1+\Delta\varphi^{\rm off}_1}. \tag{D1}$$

For the three different sets shown in Fig. 3(b) in the main text we measured low-power sets with no atoms in the cavity, and verified that $\Delta\varphi^{\rm off}_{0,1}=0$ within error bars. To be specific, we typically measure $\Delta\varphi^{\rm off}_0=0(0.25)$ mrad and $\Delta\varphi^{\rm off}_1=0(4)$ mrad, while the low-power phase shifts for $N=80\times10^3$ atoms are approximately $\Delta\varphi_0=40$ mrad and $\Delta\varphi_1=400$ mrad. Therefore, the offsets do not alter the measured ratios at the 1% level, limited by the uncertainty in our determinations of the offsets.

We consider in this case the correction factor to be $F_C=(\Delta\varphi^a_0/\Delta\varphi^a_1)/(\Delta\varphi_0/\Delta\varphi_1)$ that for small offsets $(\Delta\varphi^{\rm off}_{0,1}\ll N\Delta\varphi^a_{0,1})$ is approximately $F_C=1+((\Delta\varphi^{\rm off}_1/\Delta\varphi^a_1)-(\Delta\varphi^{\rm off}_0/\Delta\varphi^a_0))/N$. For the values just quoted and summing in quadrature the uncertainties for each phase shift, we have $F_C=1.00(1)$, which represents the largest single uncertainty contribution to the final F_C. It is worth noticing that the uncertainty in the phase shift measurements can potentially be improved by, for example, increasing the probe detunings and their power, and improving the final quantum efficiency of the detection system.

b. Axial inhomogeneous probe coupling

The optical lattice at $\lambda_{\rm trap}=813$ nm, the probe at $\lambda_1=689$ nm, and the probe at $\lambda_0=698$ nm all form standing waves in the cavity that are all incommensurate with each other. Focusing on just the two probes, the couplings vary approximately as $g^2_{0/1}=g^2_{m,0/1}\cos^2(2\pi z/\lambda_{0,1}+\psi_{0/1})$ where z is the location along the cavity axis, $z=0$ is at the center of the cavity, and the spatial phase of the standing waves is $\psi_{0/1}=0$ or $\pi/2$, depending on the relative parity of the modes. The maximum coupling at an antinode is $g^2_{0/1,m}$.

As one moves along the cavity axis, the standing wave of the two probes continuously transform every 13 μm from being aligned (having antinode aligned to antinode) to antialigned (having anitnodes aligned to nodes.) As a result, the probes do not interact with exactly the same set of atoms. However, the atoms are loaded into lattice sites spanning approximately 0.6 mm along the cavity axis (rms diameter) so that one expects the reduction in the coupling due to spatial averaging to be nearly identical and thus cancel in the ratio of the measured couplings. Assuming atoms are only located every $\lambda_{\rm trap}/2$, and are spread uniformly along 0.6 mm, the ratio of averaged couplings is modified by $<2\times10^{-3}$. If a more reasonable Gaussian envelope with standard deviation 0.3 mm (rms radius) is used to describe the loading of the lattice sites, the ratio of averaged couplings is changed by many orders of magnitude less. Here, we conservatively apply a correction $F_C=1$ with an uncertainty on F_C of 2×10^{-3}.

c. Radial inhomogeneous probe coupling

The measured phase shifts are also modified when averaging over the radial positions of the atoms due to the finite difference in the probe mode waist sizes w_0 and w_1 characterizing the $1/e^2$ in intensity radius of the Gaussian TEM_{00} probe modes (see Table II). The ratio of waists scales as $\mathrm{w}_1/\mathrm{w}_0=\lambda_1/\lambda_0\approx1-1.29\times10^{-2}$. For an atom at a distance r away from the cavity axis, the ratio of the couplings g^2_0/g^2_1 is modified by the factor f compared to its on-axis value

$$f=e^{-2(\frac{r}{\bar{\mathrm{w}}})^2(\frac{\mathrm{w}_1^2-\mathrm{w}_0^2}{\bar{\mathrm{w}}^2})}, \tag{D2}$$

where $\bar{\mathrm{w}}=\sqrt{\mathrm{w}_0\mathrm{w}_1}$ is the geometric mean of the waists. For scale, at the rms thermal radius of the atomic cloud $\sigma_r=14$ μm, the correction factor is $f=1.0007$. After averaging over the atomic radial distribution, the averaged coupling g^2_0 and g^2_1 are both reduced by about 4% but the ratio g^2_0/g^2_1 is changed by less than 10^{-4}. We expect that the rms thermal radius is common to both measurements because we do interleaved nondestructive probes and because we interpolate

to zero probe power so that any potential mechanical forces on the atoms are also interpolated to zero.

d. Finite axial confinement and resolved carrier correction

The largest systematic correction that must be applied arises from the finite localization of the atoms along the axial direction. The atoms are trapped in the Lamb-Dicke regime along the cavity axis with spacing dictated by the lattice wavelength (813 nm). The probe tones almost exclusively interact with the well-resolved motional carrier transition since $\delta_{p0} \ll \omega_z$. Lastly, because of the finite localization of the atomic wave function (i.e., finite Lamb-Dicke parameter) the effective strength of the carrier transition [i.e., the effective g_0^2 is reduced by an estimated 6.2(4)% for which we apply a correction].

In order to evaluate the apparent modification to g_0^2 from this effect, we estimate the probability distribution $P(n)$ of finding an atom in the nth axial vibrational level. The estimate is made using sideband spectroscopy measurements as shown in Fig. 4(c), following Ref. [65]. Based on this probability distribution, we calculate the average correction to g_0^2. We model the light-matter coupling as $g_0^2(\phi, \hat{z}) = g_{0,m}^2 \cos^2(k_p \hat{z} + \phi)$, where k_p is the probe wave vector, $\hat{z}$ is the harmonic oscillator position operator, $g_{0,m}$ is the value of g_0 at a probe antinode, and ϕ is a uniformly distributed phase between 0 and 2π that accounts for the inhomogeneous coupling of the trap atoms to the probe. This is justified as the probe and the axial atomic distribution are incommensurate and the beating length is much shorter than the cloud extent.

Furthermore, the radial spreading of the cloud means that each atom will have a slightly different axial trap frequency. To leading order, an atom at distance r from the center will have an axial frequency $\omega_z(r) = \omega_{z,0}[1 - (r/\mathrm{w_{trap}})^2]$, where $\omega_{z,0}$ is the maximum axial frequency [$\omega_{z,0}/2\pi = 230(1)$ kHz] and $\mathrm{w_{trap}}$ is the trap waist ($\mathrm{w_{trap}} = 79.7\ \mu$m). As both directions are decoupled, we have that the average axial frequency over the atomic ensemble is $\langle \omega_z \rangle = \omega_{z,0}[1 - (\langle r^2 \rangle / \mathrm{w_{trap}^2})]$. For a Gaussian radial density distribution profile, we have $\langle r^2 \rangle = 2\sigma_r^2 = 2k_B T_r/(m\omega_r^2)$, with T_r the radial temperature determined from the motional sideband fit, k_B is the Boltzmann constant, ω_r the radial trap frequency, and σ_r the rms thermal radius of the cloud along its radial direction.

We calculate the average value $\langle g_0^2 \rangle$ over this distribution for this effective axial trap frequency $\langle \omega_z \rangle$, that is the value that enters in our measurement result for $\Delta\varphi_0$, as

$$\langle g_0^2 \rangle = \sum_{n=0}^{n=Nz} \frac{1}{2\pi} \int_0^{2\pi} P(n)\, \langle n|\, g_{0,m}^2 \cos^2(k_p \hat{z} + \phi)\, |n\rangle\, d\phi, \tag{D3}$$

where N_z is the maximum harmonic level on the trap ($N_z \sim 17$) [65] and $|n\rangle$ are the eigenstates of the unperturbed harmonic potential along the z direction. We follow a similar procedure for the 689-nm probe, but taking into account that we are probing every transition, i.e., we sum over all possible initial and final states correcting the relative detuning between each harmonic oscillator state. Based on the reconstructed probability distribution $P(n)$, we obtain a correction factor $F_C = 1.062(4)$, dominated by the uncertainty on the fitted temperature on the axial and radial coordinates. This is the biggest correction we apply to the measured ratio $(\Delta\varphi_0/\Delta\varphi_1)$.

We emphasize that for the $^3P_1$ probe, where the probe detuning is much bigger than the trap frequency ($\delta_{C1} \gg \omega_z$), the vibrational degrees of freedom do not play a significant role. However, the average over the phase φ in Eq. (D3) gives a $\frac{1}{2}$ reduction on g_1^2, that is also present in the g_0^2 term, making this a common mode effect whose impact is highly suppressed. Imperfect cancellation of this factor is taken into account on the previous section (Appendix D 3 b).

e. Ground-state m_F distribution

The initial distribution among the different magnetic m_F sublevels in the ground states is extremely important. For example, if there are atoms in any other m_F state other than $\pm\frac{9}{2}$, both $\Delta\varphi_0$ and $\Delta\varphi_1$ (or the measured $\Delta\omega_1$) will be affected. Measuring the frequency splitting between the superradiant pulses on the clock transition [24], confirmed that the initial optical pumping efficiency is at least 95% to the $\pm\frac{9}{2}$ states. In order to estimate the correction to the dispersive phase shift ratio, we assume a conservative bound of 5% of the atoms in a wrong state. We model the measured ratio $(\Delta\varphi_0/\Delta\varphi_1)$ when 5% of the atoms are allowed to be in any of the other m_F levels as a function of the detuning δ_{C1}. Because the position of the different hyperfine levels on the $^3P_1$ state relative to the cavity modes [hyperfine splitting is comparable to cavity free spectral range, see Fig. 4(b)(ii)], and the fact that each transition has a different set of Clebsch-Gordan coefficients, the correction factor is highly sensitive to the cavity detuning δ_{C1}. A detail explanation follows below.

We consider a realization of the atomic distribution among the ground hyperfine state levels P_G that contains the list of probabilities of finding an atom in each ground state m_F. Ideally, $P_G = \{1/2, 0, \ldots, 0, 1/2\}$, for the set $m_F = \{-9/2, -7/2, \ldots, 7/2, 9/2\}$. For the phase shift on $^1S_0 \to {}^3P_0$ transition at 698 nm, $\Delta\varphi_0$, the new phase shift for an arbitrary distribution P_G on the m_F manifold is

$$\Delta\varphi_{0,\{m_F\}} = \sum_{m_F=-9/2}^{m_F=9/2} P_G(m_F) \frac{4N\left[c_\pi^0(m_F)\right]^2 g_0^2}{\kappa_0 \delta_{p0}}, \tag{D4}$$

where $c_\pi^0(m_F)$ is the Clebsch-Gordan coefficient for π-polarized light probing the m_F hyperfine ground state on the $^1S_0 \to {}^3P_0$ transition, populated with probability $P_G(m_F)$.

For the phase shift at the $^1S_0 \to {}^3P_1$ transition at 689 nm, $\Delta\varphi_1$, the equivalent modification is

$$\Delta\varphi_{1,\{m_F\}} = \sum_{k=\{0,1\}} \sum_{m_F=-9/2}^{m_F=9/2} P_G(m_F) \frac{2\pi N g_1^2}{\kappa_1} (-1)^k \left(\frac{\left[c_{\pi,9/2}^0(m_F)\right]^2}{\delta_{C1} - k \times \Delta_{\mathrm{FSR},1}} + \frac{\left[c_{\pi,11/2/2}^0(m_F)\right]^2}{\delta_{C1} - \Delta_{11/2} - k \times \Delta_{\mathrm{FSR},1}} + \frac{\left[c_{\pi,7/2}^0(m_F)\right]^2}{\delta_{C1} - \Delta_{7/2} - k \times \Delta_{\mathrm{FSR},1}} \right), \tag{D5}$$

where $c^0_{\pi,9/2}(m_F)$, $c^0_{\pi,11/2}(m_F)$, and $c^0_{\pi,7/2}(m_F)$ are the Clebsch-Gordan coefficients for the π-polarized transition on the $F = \frac{9}{2}, \frac{11}{2}, \frac{7}{2}$ hyperfine manifolds for each m_F state, populated with probability $P_G(m_F)$. Note that the sum subtracts the shifts on the two cavity modes (k index), as shown in Fig. 4(b)(ii), and the signs on $\Delta_{9/2}$ and $\Delta_{7/2}$ are taken to be consistent with the cavity detuning definition (δ_{C1}).

Corrections on the measured ratio are shown in Fig. 5(e) for the case where the fractional population on the $\pm\frac{7}{2}$ states is ε, on the $\pm\frac{5}{2}$ states is ε^2, on the $\pm\frac{3}{2}$ states is ε^3, and on the $\pm\frac{1}{2}$ states is ε^4. We determine the value of F_C as the one for $\varepsilon = 0.05$, and its uncertainty the one associated to the spread in order to cover up to $\varepsilon = 0.1$, giving $F_C = 1.001(1)$. We point out again the dependence on the cavity detuning to the $^3P_1$ manifold, δ_{C1}, on the correction factor F_C on Fig. 5(e) inset for $\varepsilon = 0.05$. For the value we choose to operate [$\delta_{C1}/(2\pi) = 277.5(8)$ MHz] we are near the maximum correction factor, but we gain in insensitivity with respect to the cavity detuning.

f. Finite lifetime on the optical lattice

Any of our measurement sequences that involve a few consecutive measurements per experimental trial are susceptible to atom loss from the trap. In particular, the lifetime in the lattice is $\tau_{\text{latt}} \sim 500$ ms (limited by parametric heating), while typical measurements on the clock transition last $T_m \sim 20$ ms typically. By combining 5 of these measurements, as in Fig. 3(b) in the main text, we can use the different outcomes and partially cancel the effect of the trap lifetime, by retaining a correction $1 + \alpha(T_m/\tau_{\text{latt}})^2$, where α can vary from 0 to 1 according to the way we combine the measurement outcomes (see next sections). The magnitude and uncertainty on the correction contemplates a uniform spread of α.

g. Cavity birefringence

In an ideal atom-cavity system, light polarized along the atoms' quantization axis will only interact with π transitions. However, the presence of cavity birefringence featuring normal modes misaligned with this axis leads to a coupling between π-polarized light and atomic transitions normally driven by circularly polarized light that is quadratic in the birefringent energy splitting. This effect introduces corrections to both phase shift measurements which do not cancel in their ratio, leading to a systematic on the ratio measurement. Calculating these corrections requires modifying the cavity transfer function shown in Eq. (A3).

In the presence of cavity birefringence, a single longitudinal mode splits into two resonances characterized by polarization eigenmodes $\hat{c}_\pm$, such that

$$\hat{H}_{\text{cav}} = \left(\omega_c - \frac{\delta_b}{2}\right)\hat{c}_-^\dagger \hat{c}_- + \left(\omega_c + \frac{\delta_b}{2}\right)\hat{c}_+^\dagger \hat{c}_+ \tag{D6}$$

for birefringent splitting δ_b. Since the probe beam polarization and quantization axis are aligned to a common vertical direction [$\hat{x}$ as in Fig. 4(a)], it makes sense to express these eigenmodes in this basis as well. This is accomplished using two parameters θ_b, φ_b:

$$\begin{aligned} \hat{c}_- &= [\cos(\theta_b/2)]\,\hat{v} + [-\sin(\theta_b/2)e^{-i\varphi_b}]\,\hat{h}, \\ \hat{c}_+ &= [\sin(\theta_b/2)e^{i\varphi_b}]\,\hat{v} + [\cos(\theta_b/2)]\,\hat{h}, \end{aligned} \tag{D7}$$

such that light along $\hat{h}$ [$\hat{y}$ as in Fig. 4(a)] and $\hat{v}$ polarizations interact with σ and π transitions, respectively. The above expressions are essentially Jones vector representations of the eigenmodes; correspondingly, θ_b and φ_b can be thought of as spherical coordinates for the eigenmodes on the Poincaré sphere with poles defined by h and v polarizations.

As long as the atoms occupy stretched states ($m_F = \pm\frac{9}{2}$), there is only one σ transition. Therefore, one can unambiguously define collective spin operators along the two transitions, denoted by $J^\pm_{\pi/\sigma} = \sum_{i=1}^N \sigma^\pm_{i,\pi/\sigma}$ and $J^z_{\pi/\sigma} = \frac{1}{2}\sum_{i=1}^N \sigma^z_{i,\pi/\sigma}$ for single-particle operators $\sigma^*_{i,\pi/\sigma}$. We go into the rotating frame of the atoms, assuming the two transitions are degenerate in frequency, to construct the following Hamiltonian:

$$\hat{H} = \left[\left(\delta_c - \frac{\delta_b}{2}\cos\theta_b\right)\hat{v}^\dagger\hat{v} + \left(\delta_c + \frac{\delta_b}{2}\cos\theta_b\right)\hat{h}^\dagger\hat{h} + \frac{\delta_b}{2}\sin\theta_b(\hat{h}^\dagger\hat{v}e^{i\varphi_b} + \hat{h}\hat{v}^\dagger e^{-i\varphi_b})\right] + [g_\pi(\hat{v}\hat{J}^+_\pi + \hat{v}^\dagger\hat{J}^-_\pi) + g_\sigma(\hat{h}\hat{J}^+_\sigma + \hat{h}^\dagger\hat{J}^-_\sigma)]. \tag{D8}$$

Analogously to the derivation at the start of this document, one can derive optical Bloch equations to analyze mean-field behavior ($O = \langle\hat{O}\rangle$). Assuming a vertically polarized cavity drive $v_i(t)$ at detuning δ_p from atomic resonance, these equations are given by

$$\begin{aligned} \dot{v} &= -i\left[\left(\delta_c - \frac{\delta_b}{2}\cos\theta_b\right)v + \left(\frac{\delta_b}{2}\sin\theta_b\, e^{-i\varphi_b}\right)h\right] - ig_\pi J^-_\pi - \frac{\kappa}{2}v + \sqrt{\kappa_m}v_i(t), \\ \dot{h} &= -i\left[\left(\delta_c + \frac{\delta_b}{2}\cos\theta_b\right)h + \left(\frac{\delta_b}{2}\sin\theta_b\, e^{i\varphi_b}\right)v\right] - ig_\sigma J^-_\sigma - \frac{\kappa}{2}h, \\ \dot{J}^-_\pi &= 2ig_\pi v J^z_\pi - \gamma^\perp_\pi J^-_\pi, \quad \dot{J}^-_\sigma = 2ig_\sigma h J^z_\sigma - \gamma^\perp_\sigma J^-_\sigma, \\ \dot{J}^z_\pi &= ig_\pi(v^\dagger J^-_\pi - vJ^+_\pi) - \gamma_\pi N_\pi, \quad \dot{J}^z_\sigma = ig_\sigma(h^\dagger J^-_\sigma - hJ^+_\sigma) - \gamma_\sigma N_\sigma, \end{aligned} \tag{D9}$$

where $N_{\pi/\sigma}$ represents the number of atoms excited along the π/σ transition. In the weak probe limit, both of these go to 0 as there are no excited atoms available to decay.

From these equations, one can determine how the input probe $v_i(t) = \tilde{v}_i e^{-i\delta_p t}$ changes in transmission through the atom-cavity system. In general for a birefringent cavity, the transmitted light's polarization may be different from the probe due to different resonance conditions for the two normal polarization modes. In our experiment, we beat the transmitted light with a vertically polarized local oscillator to measure the light in heterodyne, so the signal of interest is the vertical component of any transmitted light. We are therefore interested in the transfer function $T_v(\delta_p)$, defined by $\tilde{v}_t = T_v(\delta_p)\tilde{v}_i$. It turns out that T_v can be expressed in terms of the following transfer functions, which decouple the horizontal and vertical excitations:

$$T_\pi(\delta_p) = \frac{1}{1 - i\left(\frac{\delta_p - \delta_c + \delta_b/2\cos\theta_b}{\kappa/2}\right) + \frac{NC_\pi\gamma_\pi/2}{\gamma_\pi^\perp - i\delta_p}},$$
$$T_\sigma(\delta_p) = \frac{1}{1 - i\left(\frac{\delta_p - \delta_c - \delta_b/2\cos\theta_b}{\kappa/2}\right) + \frac{NC_\sigma\gamma_\sigma/2}{\gamma_\sigma^\perp - i\delta_p}}. \quad \text{(D10)}$$

Then, the full transfer function is given by

$$T_v(\delta_p) = \frac{T_\pi(\delta_p)}{1 + \left(\frac{\delta_b}{\kappa}\sin\theta_b\right)^2 T_\sigma(\delta_p)T_\pi(\delta_p)}. \quad \text{(D11)}$$

Note that the transfer function does not depend on the azimuthal angle φ_b; this holds as long as the transmitted light is only measured along v. For small birefringent splitting, F_v can be calculated perturbatively by expanding in powers of $(\frac{\delta_b}{\kappa}\sin\theta_b)^2$. It follows that leading-order corrections to the cavity shifts will be quadratic in δ_b.

Using a simple polarimetry setup consisting of PBSs, waveplates, and photodiodes, we were able to measure $\delta_{b0}/\kappa_0 = +0.16(2)$, $\delta_{b1}/\kappa_1 = +0.16(2)$, and $\theta_b = 30(2)^\circ$. This implies $(\frac{\delta_b}{\kappa}\sin\theta_b)^2 = 0.006(2)$ along both transitions, justifying a perturbative treatment. From this, we can calculate the modified shifts and derive a correction factor for the shift ratio $\Delta\varphi_0/\Delta\varphi_1$, which turns out to be $F_C = 1.012(3)$. This value accounts for all differential shift measurements, as well as the full hyperfine landscape.

Considering the effect of cavity birefringence opens up new potential sources of uncertainty. First, one might imagine that an imperfect optical pumping scheme might conspire with the cavity's birefringence to produce larger corrections than previously discussed. In fact, numerical calculations show the two effects are largely decoupled and can be treated separately. Second, if the local oscillator is misaligned from vertical polarization by some small angle α, all phase shifts will receive a linear correction proportional to $\alpha\frac{\delta_b}{\kappa}\sin\theta_b$. However, the experiment's differential probe design leads to partial cancellation of these shifts. Assuming α is uncertain by 5°, the additional uncertainty on F_C is at most 0.003. Finally, if the two birefringent normal modes exhibit slightly different linewidths, the optical Bloch equations change accordingly and lead to further phase shift modifications. Data used to determine δ_b allows us to constrain any linewidth difference to $\delta\kappa \lesssim 0.05\kappa$, which limits the correction on F_C to $\lesssim 0.001$. Incorporating these additional sources of uncertainty into the birefringence correction factor gives $F_C = 1.012(5)$.

This experiment was performed before the discovery of cavity birefringence in our system. In principle, for future experiments one could mitigate the effect of this systematic by aligning all beam polarizations and the atoms' quantization axis along the birefringent eigenmode axis. If the eigenmodes are linearly polarized, the probe beam will only excite one of the two modes, completely removing any birefringent coupling. Otherwise, any ellipticity the eigenmodes possess will limit the ability to suppress the coupling with a linearly polarized probe beam, which is necessary for this experiment. In our system, the effect of birefringence could be suppressed by approximately ~17 by such an alignment.

4. Summary: Full systematic correction

Taking all these effects into account we infer a correction factor $F_C = 1.074(16)$ on the measured ratio $(\Delta\varphi_0/\Delta\varphi_1)$. Its value is determined by multiplying the systematic corrections detailed in Tables III, IV, and V, while its uncertainty is properly summed in quadrature. The uncertainty on F_C is dominated, mostly, by technical issues, such as the uncertainty in the clock atomic frequency, the cavity alignment with the atomic resonance, and alignment of the probe polarization with respect to the cavity eigenmode axis considering birefringence, which can be further improved. Furthermore, its uncertainty is also dominated by technical aspects such as signal to noise in our data and its influence on determining the phase shift offsets, as well as uncertainty in the atomic transition frequency and cavity alignment on the clock transition.

APPENDIX E: EXTRAPOLATING $\Delta\varphi_0/\Delta\varphi_1$ TO ZERO-PROBE POWER AND INTERLEAVED MEASUREMENTS

In this Appendix, we will discuss the details of the low-power measurement presented in Fig. 3(b) in the main text. Absent systematic corrections, it remains to determine the zero-probe-power value for the ratio $(\Delta\varphi_0/\Delta\varphi_1)$, that we will name $(\Delta\varphi_0/\Delta\varphi_1)_{P=0}$.

We measured the ratio of the atomic phase shift to cavity frequency shift while simultaneously decreasing both 698 and 689 probe powers, P_0 and P_1, respectively, and taking longer sets to accumulate similar statistics for lower optical power measurements, as expected from the photon-shot-noise scaling. The ratio is expected to strongly depend on both powers, although the maximum 689-nm optical power was already low enough to be a significant effect, according to the results shown in Figs. 5(b) and 5(c). We measure $\Delta\varphi_0$ and $\Delta\varphi_1$ in an interleave form, to gain insensitivity with respect to lattice lifetime. We realize five measurements every $T_c = 25$ ms, as shown in Fig. 3(b) in the main text, interleaving three $\Delta\varphi_1$ short measurements (~2 ms) with two longer $\Delta\varphi_0$ measurements (~25 ms). Upon further detailed inspection, the ratio of the average of two $\Delta\varphi_0$'s and the average of the three $\Delta\varphi_1$'s measurements will have the same linear sensitivity to

TABLE VI. This table contains different fits for several estimators for the ratio $(\Delta\varphi_0/\Delta\varphi_1)$.

Estimator	Fit method/origin	$\left(\frac{\Delta\varphi_0}{\Delta\varphi_1}\right)_{P=0} \times 10^{-2}$	χ^2_ν
Estimator E_1	Quadratic on P_0. Mean value for crossing	−8.92(6)	
Estimator E_2	Quadratic on P_0. Mean value for crossing	−8.92(6)	
Estimator E_3	Quadratic on P_0. Mean value for crossing	−8.95(6)	
Estimator E_3	Linear on P_0 ($P_0 \leqslant 400$ pW). Mean value for crossing	−8.95(6)	
Estimator E_3 removing 7 ms data	Quadratic on P_0. Mean value for crossing	−8.95(6)	
Estimator E_3 only for red set	Quadratic on P_0	−8.86(6)	0.7
Estimator E_3 only for green set	Quadratic on P_0	−9.02(7)	1.2
Estimator E_3 only for blue set	Quadratic on P_0	−8.95(4)	0.6
Estimator E_3	Quadratic on P_0. Using a global fit to the three sets	−8.95(4)	1.1

atom loss, therefore, a ratio of the two quantities will be quadratically sensitive to T_c/τ_{latt}.

The 698-nm clock transition probe could excite atoms to $|e_0\rangle$, and those atoms will not be counted by the following dispersive 689-nm probe. We assume, in the weak probe power limit, that each clock transition probe excites a fraction β_0 of atoms into $|e_0\rangle$ every $T_c/2$ interval while they are being probed. Reversely, if there are atoms in the excited state, a fraction β_0 is transferred to $|g\rangle$. For the 689-nm probe, we assume an excitation fraction β_1, but also that any atom in the excited state is reset to the ground state before the following $\Delta\varphi_0$ measurement, as the spontaneous emission decay time is only 21 μs. Furthermore, losses from the lattice are treated as an exponential loss decay with time constant τ_{latt}, which was experimentally verified repeatedly.

We use the measurement outcomes of the different $\Delta\varphi_0$ and $\Delta\varphi_1$ measurements to construct different estimators for the zero-power ratio $(\Delta\varphi_0/\Delta\varphi_1)_{P=0}$. Examples of these estimators, to name a few, are

$$E_1 = \frac{3}{2}\left(\frac{\Delta\varphi_0^1 + \Delta\varphi_0^2}{\Delta\varphi_1^1 + \Delta\varphi_1^2 + \Delta\varphi_1^3}\right), \tag{E1}$$

$$E_2 = 2\left(\frac{\Delta\varphi_0^1 + \Delta\varphi_0^2}{\Delta\varphi_1^1 + 2\Delta\varphi_1^2 + \Delta\varphi_1^3}\right), \tag{E2}$$

$$E_3 = 4\left(\frac{\Delta\varphi_0^1 + \Delta\varphi_0^2}{\Delta\varphi_1^1 + 6\Delta\varphi_1^1 + \Delta\varphi_1^3}\right), \tag{E3}$$

where the superindex orders each of the five measurements, i.e., $\Delta\varphi_1^2$ is the second $\Delta\varphi_1$ measurement.

For low optical power β_0 (β_1) is proportional to the probe optical power P_0 (P_1) on the clock transition (7.5-kHz transition) and satisfies β_0 (β_1) $\ll 1$. In this case we can compute how populating the $|e_0\rangle$ and $|e_1\rangle$ states during the measurement sequence affects the estimators, for example,

$$\begin{aligned}
E_1 &= \left(\frac{\Delta\varphi_0}{\Delta\varphi_1}\right)_{P=0}\left(1 - \beta_0 + 2\beta_1 - \frac{5}{6}(T_c/\tau_{\text{latt}})^2 + O(\beta_0, \beta_1, T_c/\tau_{\text{latt}})\right),\\
E_2 &= \left(\frac{\Delta\varphi_0}{\Delta\varphi_1}\right)_{P=0}\left(1 - \beta_0 + 2\beta_1 - \frac{1}{2}(T_c/\tau_{\text{latt}})^2 + O(\beta_0, \beta_1, T_c/\tau_{\text{latt}})\right),\\
E_3 &= \left(\frac{\Delta\varphi_0}{\Delta\varphi_1}\right)_{P=0}[1 - \beta_0 + 2\beta_1 + O(\beta_0, \beta_1, T_c/\tau_{\text{latt}})],
\end{aligned} \tag{E4}$$

where $O(\beta_0, \beta_1, T_c/\tau_{\text{latt}})$ refers to higher-order terms in combinations of β_0, β_1, and T_c/τ_{latt}, and $(\frac{\Delta\varphi_0}{\Delta\varphi_1})_{P=0}$ is the zero-power ratio that we want to determine.

In Fig. 3(b) in the main text we show the result for the so-called E_3 estimator above and show quadratic polynomial fits in the optical power P_0 for the clock transition ($\beta_0 \propto P_0$). In Table VI we show the fitted $(\frac{\Delta\varphi_0}{\Delta\varphi_1})_{P=0}$ for different estimators and fit methods, as a way to show a consistent method-independent value. The data are not corrected by any systematic. We also point out that we did not take β_1 or P_1 into consideration for either of these fits, as doing so does not significantly modify the other fitted parameters, because the maximum value that P_1 takes on all the Fig. 3(b) measurements is already low enough to cause significant population in $|e_1\rangle$.

The results are consistent with a zero-power crossing $(\frac{\Delta\varphi_0}{\Delta\varphi_1})_{P=0} = -8.95(9) \times 10^{-2}$. We finally note that for single measurement instances as represented by the red, green, and blue data sets, independently of the estimators we compute, the data are spread consistently with a 10-kHz uncertainty on the alignment of the cavity resonance frequency to the clock atomic transition (δ_{C0}), as described previously. A zoom-in of the data presented in Fig. 3(b) in the main text is shown in Fig. 5(f). Fits are for the estimator E_3 for each set, and the black solid line is a global fit for all the data sets.

APPENDIX F: EXTRACTING γ_0/γ_1 FROM THE MEASURED $\Delta\varphi_0/\Delta\varphi_1$

In order to extract the ratio between $(g_0/g_1)^2$, which in conjunction with the known $^3P_1$ linewidth [75] could determine the $^3P_0$ natural radiative linewidth, we use Eqs. (C1) and (C2), the systematic correction F_C, and the measured value for $(\Delta\varphi_0/\Delta\varphi_1)_{P=0}$ from the zero-power crossing measurement. Furthermore, we need to determine all the numerical factors that appear in Eqs. (C1) and (C2) with their uncertainty. Most of these factors were already described above and appear on Table II.

We obtain $(\Delta\varphi_0/\Delta\varphi_1)_{P=0} = -9.61(17) \times 10^{-2}$ after applying the systematic correction factor F_C, adding both statistical and systematic uncertainty contributions in quadrature. Using Eqs. (C1) and (C2), we determine $(g_0/g_1)^2 = 1.83(3) \times 10^{-7}$.

The radiative excited-state linewidths are $\gamma_0 \propto d_0^2(\omega_{A0})^3$ and $\gamma_1 \propto d_1^2(\omega_{A1})^3$ [88,89], where d_0 and d_1 are the electric dipole moments between the $^1S_0$ and the $^3P_0$ state, and the $^1S_0$ and the $^3P_1$ state, respectively. On the other hand, $g_0 \propto d_0\sqrt{\frac{\omega_{A0}}{w_0^2 L_0}}$ and $g_1 \propto d_1\sqrt{\frac{\omega_{A1}}{w_1^2 L_1}}$ for the same pair of transitions [61–63]. Here, $w_{0,1}$ and $L_{0,1}$ refer to the cavity mode waist ($1/e^2$ radio) and cavity length for the same transitions as before. All the numerical proportionality constants that we are omitting are physical constants, independent of the transitions we use. Finally, we have

$$\frac{\gamma_0}{\gamma_1} = \left(\frac{g_0}{g_1}\right)^2 \left(\frac{w_0}{w_1}\right)^2 \left(\frac{\omega_{A0}}{\omega_{A1}}\right)^2 \frac{L_0}{L_1}. \tag{F1}$$

Using the values measured in this work and the best reported value for γ_1 to our knowledge [75], we report $\gamma_0/(2\pi) = 1.35 \pm 0.03$ mHz, that implies a lifetime of 118 ± 3 s.

APPENDIX G: CONSTRAINING N-DEPENDENT EFFECTS ON $\Delta\varphi_0/\Delta\varphi_1$ MEASUREMENTS

As discussed on a few of the systematic corrections presented previously, sometimes we can find atom-number-dependent corrections that do not completely cancel when measuring the ratio $\Delta\varphi_0/\Delta\varphi_1$, for example, when discussing the independent phase shift offsets or higher-order corrections.

In order to check the influence of these effects, and lacking an underlying model to believe they would impact our measurement, we decided to perform $\Delta\varphi_0/\Delta\varphi_1$ measurements for different atom number N. These measurements are presented as an inset in Fig. 3(b) in the main text.

For that set, our phase shift measurements present some nonzero phase shift offsets that were properly measured. The most simplistic model, as introduced in Eq. (D1), serves us as a proxy to further investigate any unknown variations with N and $1/N$ on the ratio measurements. All in all, by considering different variations of these fits, taking into account the $N = 0$ point and the offsets we measured, we find agreement at the 2% level with the weighed average of the measured phase shift ratio (the value that we would assign for the ratio if no N-dependent effect were present). This uncertainty is dominated by the signal-to-noise ratio on the current data set.

Therefore, we constrain any unknown N-dependent effect on the ratio at the 2% level, which is at the level of our final uncertainty on the phase shift ratio and linewidth ratio. We consider this experiment as a sanity check, but we do not use this independent constraint to modify our final uncertainty.

[1] A. D. Ludlow, M. M. Boyd, J. Ye, E. Peik, and P. O. Schmidt, Optical atomic clocks, Rev. Mod. Phys. **87**, 637 (2015).

[2] E. Oelker, R. B. Hutson, C. J. Kennedy, L. Sonderhouse, T. Bothwell, A. Goban, D. Kedar, C. Sanner, J. M. Robinson, G. E. Marti, D. G. Matei, T. Legero, M. Giunta, R. Holzwarth, F. Riehle, U. Sterr, and J. Ye, Demonstration of 4.8×10^{17} stability at 1s for two independent optical clocks, Nat. Photonics **13**, 714 (2019).

[3] S. L. Campbell, R. B. Hutson, G. E. Marti, A. Goban, N. Darkwah Oppong, R. L. McNally, L. Sonderhouse, J. M. Robinson, W. Zhang, B. J. Bloom, and J. Ye, A fermi-degenerate three-dimensional optical lattice clock, Science **358**, 90 (2017).

[4] I. Ushijima, M. Takamoto, M. Das, T. Ohkubo, and H. Katori, Cryogenic optical lattice clocks, Nat. Photonics **9**, 185 (2015).

[5] T. Takano, M. Takamoto, I. Ushijima, N. Ohmae, T. Akatsuka, A. Yamaguchi, Y. Kuroishi, H. Munekane, B. Miyahara, and H. Katori, Geopotential measurements with synchronously linked optical lattice clocks, Nat. Photonics **10**, 662 (2016).

[6] J. Grotti, S. Koller, S. Vogt, S. Häfner, U. Sterr, C. Lisdat, H. Denker, C. Voigt, L. Timmen, A. Rolland, F. N. Baynes, H. S. Margolis, M. Zampaolo, P. Thoumany, M. Pizzocaro, B. Rauf, F. Bregolin, A. Tampellini, P. Barbieri, M. Zucco *et al.*, Geodesy and metrology with a transportable optical clock, Nat. Phys. **14**, 437 (2018).

[7] M. Schioppo, R. C. Brown, W. F. McGrew, N. Hinkley, R. J. Fasano, K. Beloy, T. H. Yoon, G. Milani, D. Nicolodi, J. A. Sherman, N. B. Phillips, C. W. Oates, and A. D. Ludlow, Ultrastable optical clock with two cold-atom ensembles, Nat. Photonics **11**, 48 (2016).

[8] S. M. Brewer, J.-S. Chen, A. M. Hankin, E. R. Clements, C. W. Chou, D. J. Wineland, D. B. Hume, and D. R. Leibrandt, $^{27}Al^+$ Quantum-Logic Clock with a Systematic Uncertainty Below 10^{-18}, Phys. Rev. Lett. **123**, 033201 (2019).

[9] M. S. Safronova, D. Budker, D. DeMille, D. F. J. Kimball, A. Derevianko, and C. W. Clark, Search for new physics with atoms and molecules, Rev. Mod. Phys. **90**, 025008 (2018).

[10] G. M. Tino, A. Bassi, G. Bianco, K. Bongs, P. Bouyer, L. Cacciapuoti, S. Capozziello, X. Chen, M. L. Chiofalo, A. Derevianko, W. Ertmer, N. Gaaloul, P. Gill, P. W. Graham, J. M. Hogan, L. Iess, M. A. Kasevich, H. Katori, C. Klempt, X. Lu *et al.*, Sage: A proposal for a space atomic gravity explorer, Eur. Phys. J. D **73**, 228 (2019).

[11] L. Hu, N. Poli, L. Salvi, and G. M. Tino, Atom Interferometry with the Sr Optical Clock Transition, Phys. Rev. Lett. **119**, 263601 (2017).

[12] R. P. del Aguila, T. Mazzoni, L. Hu, L. Salvi, G. M. Tino, and N. Poli, Bragg gravity-gradiometer using the $^1S_0 - {}^3P_1$ intercombination transition of ^{88}Sr, New J. Phys. **20**, 043002 (2018).

[13] A. Arvanitaki, P. W. Graham, J. M. Hogan, S. Rajendran, and K. Van Tilburg, Search for light scalar dark matter with atomic gravitational wave detectors, Phys. Rev. D **97**, 075020 (2018).

[14] P. Wcisło, P. Ablewski, K. Beloy, S. Bilicki, M. Bober, R. Brown, R. Fasano, R. Ciuryło, H. Hachisu, T. Ido *et al.*, New bounds on dark matter coupling from a global network of optical atomic clocks, Sci. Adv. **4**, eaau4869 (2018).

[15] C. J. Kennedy, E. Oelker, J. M. Robinson, T. Bothwell, D. Kedar, W. R. Milner, G. E. Marti, A. Derevianko, and J. Ye, Precision Metrology Meets Cosmology: Improved Constraints on Ultralight Dark Matter from Atom-Cavity Frequency Comparisons, Phys. Rev. Lett. **125**, 201302 (2020).

[16] M. Abe, P. Adamson, M. Borcean, D. Bortoletto, K. Bridges, S. P. Carman, S. Chattopadhyay, J. Coleman, N. M. Curfman, K. DeRose *et al.*, Matter-wave atomic gradiometer interferometric sensor (MAGIS-100), Quantum Science and Technology.

[17] M. A. Norcia, R. J. Lewis-Swan, J. R. K. Cline, B. Zhu, A. M. Rey, and J. K. Thompson, Cavity-mediated collective spin-exchange interactions in a strontium superradiant laser, Science **361**, 259 (2018).

[18] J. A. Muniz, D. Barberena, R. J. Lewis-Swan, D. J. Young, J. R. K. Cline, A. M. Rey, and J. K. Thompson, Exploring dynamical phase transitions with cold atoms in an optical cavity, Nature (London) **580**, 602 (2020).

[19] S. Kolkowitz, S. L. Bromley, T. Bothwell, M. L. Wall, G. E. Marti, A. P. Koller, X. Zhang, A. M. Rey, and J. Ye, Spin-orbit-coupled fermions in an optical lattice clock, Nature (London) **542**, 66 (2016).

[20] S. L. Bromley, S. Kolkowitz, T. Bothwell, D. Kedar, A. Safavi-Naini, M. L. Wall, C. Salomon, A. M. Rey, and J. Ye, Dynamics of interacting fermions under spin-orbit coupling in an optical lattice clock, Nat. Phys. **14**, 399 (2018).

[21] A. Goban, R. B. Hutson, G. E. Marti, S. L. Campbell, M. A. Perlin, P. S. Julienne, J. P. D'Incao, A. M. Rey, and J. Ye, Emergence of multi-body interactions in a fermionic lattice clock, Nature (London) **563**, 369 (2018).

[22] R. Senaratne, S. V. Rajagopal, T. Shimasaki, P. E. Dotti, K. M. Fujiwara, K. Singh, Z. A. Geiger, and D. M. Weld, Quantum simulation of ultrafast dynamics using trapped ultracold atoms, Nat. Commun. **9**, 2065 (2018).

[23] M. A. Norcia, M. N. Winchester, J. R. K. Cline, and J. K. Thompson, Superradiance on the millihertz linewidth strontium clock transition, Sci. Adv. **2**, e1601231 (2016).

[24] M. A. Norcia, J. R. K. Cline, J. A. Muniz, J. M. Robinson, R. B. Hutson, A. Goban, G. E. Marti, J. Ye, and J. K. Thompson, Frequency Measurements of Superradiance from the Strontium Clock Transition, Phys. Rev. X **8**, 021036 (2018).

[25] E. Pedrozo-Peñafiel, S. Colombo, C. Shu, A. F. Adiyatullin, Z. Li, E. Mendez, B. Braverman, A. Kawasaki, D. Akamatsu, Y. Xiao, and V. Vuletić, Entanglement on an optical atomic-clock transition, Nature (London) **588**, 414 (2020).

[26] M. J. Martin, D. Meiser, J. W. Thomsen, J. Ye, and M. J. Holland, Extreme nonlinear response of ultranarrow optical transitions in cavity qed for laser stabilization, Phys. Rev. A **84**, 063813 (2011).

[27] B. T. R. Christensen, M. R. Henriksen, S. A. Schäffer, P. G. Westergaard, D. Tieri, J. Ye, M. J. Holland, and J. W. Thomsen, Nonlinear spectroscopy of Sr atoms in an optical cavity for laser stabilization, Phys. Rev. A **92**, 053820 (2015).

[28] S. A. Schäffer, B. T. R. Christensen, M. R. Henriksen, and J. W. Thomsen, Dynamics of bad-cavity-enhanced interaction with cold Sr atoms for laser stabilization, Phys. Rev. A **96**, 013847 (2017).

[29] M. N. Winchester, M. A. Norcia, J. R. K. Cline, and J. K. Thompson, Magnetically Induced Optical Transparency on a Forbidden Transition in Strontium for Cavity-Enhanced Spectroscopy, Phys. Rev. Lett. **118**, 263601 (2017).

[30] D. Meiser, J. Ye, D. R. Carlson, and M. J. Holland, Prospects for a Millihertz-Linewidth Laser, Phys. Rev. Lett. **102**, 163601 (2009).

[31] J. Chen, Active optical clock, Chin. Sci. Bull. **54**, 348 (2009).

[32] S. A. Schäffer, M. Tang, M. R. Henriksen, A. A. Jørgensen, B. T. R. Christensen, and J. W. Thomsen, Lasing on a narrow transition in a cold thermal strontium ensemble, Phys. Rev. A **101**, 013819 (2020).

[33] J. Lodewyck, P. G. Westergaard, and P. Lemonde, Nondestructive measurement of the transition probability in a Sr optical lattice clock, Phys. Rev. A **79**, 061401(R) (2009).

[34] J.-B. Béguin, E. M. Bookjans, S. L. Christensen, H. L. Sørensen, J. H. Müller, E. S. Polzik, and J. Appel, Generation and Detection of a Sub-Poissonian Atom Number Distribution in a One-Dimensional Optical Lattice, Phys. Rev. Lett. **113**, 263603 (2014).

[35] M. A. Norcia and J. K. Thompson, Strong coupling on a forbidden transition in strontium and nondestructive atom counting, Phys. Rev. A **93**, 023804 (2016).

[36] G. Vallet, E. Bookjans, U. Eismann, S. Bilicki, R. L. Targat, and J. Lodewyck, A noise-immune cavity-assisted non-destructive detection for an optical lattice clock in the quantum regime, New J. Phys. **19**, 083002 (2017).

[37] R. Hobson, W. Bowden, A. Vianello, I. R. Hill, and P. Gill, Cavity-enhanced non-destructive detection of atoms for an optical lattice clock, Opt. Express **27**, 37099 (2019).

[38] W. Bowden, A. Vianello, I. R. Hill, M. Schioppo, and R. Hobson, Improving the Q Factor of an Optical Atomic Clock Using Quantum Nondemolition Measurement, Phys. Rev. X **10**, 041052 (2020).

[39] B. Braverman, A. Kawasaki, E. Pedrozo-Peñafiel, S. Colombo, C. Shu, Z. Li, E. Mendez, M. Yamoah, L. Salvi, D. Akamatsu, Y. Xiao, and V. Vuletić, Near-Unitary Spin Squeezing in ^{171}Yb, Phys. Rev. Lett. **122**, 223203 (2019).

[40] M. Yasuda and H. Katori, Lifetime Measurement of the $^3P_2$ Metastable State of Strontium Atoms, Phys. Rev. Lett. **92**, 153004 (2004).

[41] B. B. Jensen, H. Ming, P. G. Westergaard, K. Gunnarsson, M. H. Madsen, A. Brusch, J. Hald, and J. W. Thomsen, Experimental Determination of the ^{24}Mg I $(3s3p)^3P_2$ Lifetime, Phys. Rev. Lett. **107**, 113001 (2011).

[42] T. Rosenband, P. O. Schmidt, D. B. Hume, W. M. Itano, T. M. Fortier, J. E. Stalnaker, K. Kim, S. A. Diddams, J. C. J. Koelemeij, J. C. Bergquist, and D. J. Wineland, Observation of the $^1S_0 \rightarrow {}^3P_0$ Clock Transition in $^{27}Al^+$, Phys. Rev. Lett. **98**, 220801 (2007).

[43] P. A. Barton, C. J. S. Donald, D. M. Lucas, D. A. Stevens, A. M. Steane, and D. N. Stacey, Measurement of the life-

time of the $3d^2D_{5/2}$ state in $^{40}Ca^+$, Phys. Rev. A **62**, 032503 (2000).

[44] P. Staanum, I. S. Jensen, R. G. Martinussen, D. Voigt, and M. Drewsen, Lifetime measurement of the metastable $3d^2D_{5/2}$ state in the $^{40}Ca^+$ ion using the shelving technique on a few-ion string, Phys. Rev. A **69**, 032503 (2004).

[45] A. Kreuter, C. Becher, G. P. T. Lancaster, A. B. Mundt, C. Russo, H. Häffner, C. Roos, J. Eschner, F. Schmidt-Kaler, and R. Blatt, Spontaneous Emission Lifetime of a Single Trapped Ca^+ Ion in a High Finesse Cavity, Phys. Rev. Lett. **92**, 203002 (2004).

[46] T. Becker, J. v. Zanthier, A. Y. Nevsky, C. Schwedes, M. N. Skvortsov, H. Walther, and E. Peik, High-resolution spectroscopy of a single In^+ ion: Progress towards an optical frequency standard, Phys. Rev. A **63**, 051802(R) (2001).

[47] M. Walhout, A. Witte, and S. L. Rolston, Precision Measurement of the Metastable $6s[3/2]_2$ lifetime in Xenon, Phys. Rev. Lett. **72**, 2843 (1994).

[48] M. Walhout, U. Sterr, A. Witte, and S. L. Rolston, Lifetime of the metastable $6s'[1/2]_0$ clock state in Xenon, Opt. Lett. **20**, 1192 (1995).

[49] S. Dörscher, R. Schwarz, A. Al-Masoudi, S. Falke, U. Sterr, and C. Lisdat, Lattice-induced photon scattering in an optical lattice clock, Phys. Rev. A **97**, 063419 (2018).

[50] R. B. Hutson, A. Goban, G. E. Marti, L. Sonderhouse, C. Sanner, and J. Ye, Engineering Quantum States of Matter for Atomic Clocks in Shallow Optical Lattices, Phys. Rev. Lett. **123**, 123401 (2019).

[51] S. Origlia, M. S. Pramod, S. Schiller, Y. Singh, K. Bongs, R. Schwarz, A. Al-Masoudi, S. Dörscher, S. Herbers, S. Häfner, U. Sterr, and C. Lisdat, Towards an optical clock for space: Compact, high-performance optical lattice clock based on bosonic atoms, Phys. Rev. A **98**, 053443 (2018).

[52] R. X. Schüssler, H. Bekker, M. Braß, H. Cakir, J. R. Crespo López-Urrutia, M. Door, P. Filianin, Z. Harman, M. W. Haverkort, W. J. Huang, P. Indelicato, C. H. Keitel, C. M. König, K. Kromer, M. Müller, Y. N. Novikov, A. Rischka, C. Schweiger, S. Sturm, S. Ulmer *et al.*, Detection of metastable electronic states by Penning trap mass spectrometry, Nature (London) **581**, 42 (2020).

[53] M. M. Boyd, T. Zelevinsky, A. D. Ludlow, S. Blatt, T. Zanon-Willette, S. M. Foreman, and J. Ye, Nuclear spin effects in optical lattice clocks, Phys. Rev. A **76**, 022510 (2007).

[54] S. G. Porsev and A. Derevianko, Hyperfine quenching of the metastable $^3P_{0,2}$ states in divalent atoms, Phys. Rev. A **69**, 042506 (2004).

[55] R. Santra, K. V. Christ, and C. H. Greene, Properties of metastable alkaline-earth-metal atoms calculated using an accurate effective core potential, Phys. Rev. A **69**, 042510 (2004).

[56] M. A. Norcia, A. W. Young, W. J. Eckner, E. Oelker, J. Ye, and A. M. Kaufman, Seconds-scale coherence on an optical clock transition in a tweezer array, Science **366**, 93 (2019).

[57] I. S. Madjarov, A. Cooper, A. L. Shaw, J. P. Covey, V. Schkolnik, T. H. Yoon, J. R. Williams, and M. Endres, An Atomic-Array Optical Clock with Single-Atom Readout, Phys. Rev. X **9**, 041052 (2019).

[58] D. G. Matei, T. Legero, S. Häfner, C. Grebing, R. Weyrich, W. Zhang, L. Sonderhouse, J. M. Robinson, J. Ye, F. Riehle, and U. Sterr, 1.5 μm Lasers with Sub-10 mhz Linewidth, Phys. Rev. Lett. **118**, 263202 (2017).

[59] W. Zhang, J. M. Robinson, L. Sonderhouse, E. Oelker, C. Benko, J. L. Hall, T. Legero, D. G. Matei, F. Riehle, U. Sterr, and J. Ye, Ultrastable Silicon Cavity in a Continuously Operating Closed-Cycle Cryostat at 4 K, Phys. Rev. Lett. **119**, 243601 (2017).

[60] J. M. Robinson, E. Oelker, W. R. Milner, W. Zhang, T. Legero, D. G. Matei, F. Riehle, U. Sterr, and J. Ye, Crystalline optical cavity at 4 K with thermal-noise-limited instability and ultralow drift, Optica **6**, 240 (2019).

[61] H. Tanji-Suzuki, I. D. Leroux, M. H. Schleier-Smith, M. Cetina, A. T. Grier, J. Simon, and V. Vuletić, Interaction between atomic ensembles and optical resonators: Classical description, in *Advances in Atomic, Molecular, and Optical Physics*, Advances in Atomic, Molecular, and Optical Physics, Vol. 60, edited by P. B. E. Arimondo and C. Lin (Academic, New York, 2011), Chap. 4, pp. 201–237.

[62] E. Jaynes and F. Cummings, Comparison of quantum and semiclassical radiation theories with application to the beam maser, Proc. IEEE **51**, 89 (1963).

[63] H. J. Kimble, Strong interactions of single atoms and photons in cavity QED, Phys. Scr. **1998**, 127 (1998).

[64] J. Ye, H. J. Kimble, and H. Katori, Quantum state engineering and precision metrology using state-insensitive light traps, Science **320**, 1734 (2008).

[65] S. Blatt, J. W. Thomsen, G. K. Campbell, A. D. Ludlow, M. D. Swallows, M. J. Martin, M. M. Boyd, and J. Ye, Rabi spectroscopy and excitation inhomogeneity in a one-dimensional optical lattice clock, Phys. Rev. A **80**, 052703 (2009).

[66] Z. Chen, J. G. Bohnet, J. M. Weiner, K. C. Cox, and J. K. Thompson, Cavity-aided nondemolition measurements for atom counting and spin squeezing, Phys. Rev. A **89**, 043837 (2014).

[67] V. B. Braginsky and F. Y. Khalili, Quantum nondemolition measurements: the route from toys to tools, Rev. Mod. Phys. **68**, 1 (1996).

[68] J. Appel, P. J. Windpassinger, D. Oblak, U. B. Hoff, N. Kjærgaard, and E. S. Polzik, Mesoscopic atomic entanglement for precision measurements beyond the standard quantum limit, Proc. Natl. Acad. Sci. USA **106**, 10960 (2009).

[69] Z. Chen, J. G. Bohnet, S. R. Sankar, J. Dai, and J. K. Thompson, Conditional Spin Squeezing of a Large Ensemble Via the Vacuum Rabi Splitting, Phys. Rev. Lett. **106**, 133601 (2011).

[70] M. H. Schleier-Smith, I. D. Leroux, and V. Vuletić, States of an Ensemble of Two-Level Atoms with Reduced Quantum Uncertainty, Phys. Rev. Lett. **104**, 073604 (2010).

[71] J. G. Bohnet, K. C. Cox, M. A. Norcia, J. M. Weiner, Z. Chen, and J. K. Thompson, Reduced spin measurement back-action for a phase sensitivity ten times beyond the standard quantum limit, Nat. Photonics **8**, 731 (2014).

[72] O. Hosten, N. J. Engelsen, R. Krishnakumar, and M. A. Kasevich, Measurement noise 100 times lower than the quantum-projection limit using entangled atoms, Nature (London) **529**, 505 (2016).

[73] K. C. Cox, G. P. Greve, J. M. Weiner, and J. K. Thompson, Deterministic Squeezed States with Collective Measurements and Feedback, Phys. Rev. Lett. **116**, 093602 (2016).

[74] A. Yariv, *Optical Electronics* (Saunders College, Philadelphia, 1991).

[75] T. L. Nicholson, S. L. Campbell, R. B. Hutson, G. E. Marti, B. J. Bloom, R. L. McNally, W. Zhang, M. D. Barrett, M. S. Safronova, G. F. Strouse, W. L. Tew, and J. Ye, Systematic evaluation of an atomic clock at 2×10^{-18} total uncertainty, Nat. Commun. **6**, 6896 (2015).

[76] R. Drozdowski, M. Ignaciuk, J. Kwela, and J. Heldt, Radiative lifetimes of the lowest $^3P_1$ metastable states of Ca and Sr, Z. Phys. D: Atoms, Molecules and Clusters **41**, 125 (1997).

[77] T. Zelevinsky, M. M. Boyd, A. D. Ludlow, T. Ido, J. Ye, R. Ciuryło, P. Naidon, and P. S. Julienne, Narrow Line Photoassociation in an Optical Lattice, Phys. Rev. Lett. **96**, 203201 (2006).

[78] A. V. Taichenachev, V. I. Yudin, C. W. Oates, C. W. Hoyt, Z. W. Barber, and L. Hollberg, Magnetic Field-Induced Spectroscopy of Forbidden Optical Transitions with Application to Lattice-Based Optical Atomic Clocks, Phys. Rev. Lett. **96**, 083001 (2006).

[79] E. Peik and C. Tamm, Nuclear laser spectroscopy of the 3.5 eV transition in Th-229, Europhys. Lett. **61**, 181 (2003).

[80] L. von der Wense, B. Seiferle, M. Laatiaoui, J. B. Neumayr, H.-J. Maier, H.-F. Wirth, C. Mokry, J. Runke, K. Eberhardt, C. E. Düllmann, N. G. Trautmann, and P. G. Thirolf, Direct detection of the ^{229}Th nuclear clock transition, Nature (London) **533**, 47 (2016).

[81] B. Seiferle, L. von der Wense, P. V. Bilous, I. Amersdorffer, C. Lemell, F. Libisch, S. Stellmer, T. Schumm, C. E. Düllmann, A. Pálffy, and P. G. Thirolf, Energy of the ^{229}Th nuclear clock transition, Nature (London) **573**, 243 (2019).

[82] V. A. Dzuba, A. Derevianko, and V. V. Flambaum, High-precision atomic clocks with highly charged ions: Nuclear-spin-zero f^{12}-shell ions, Phys. Rev. A **86**, 054501 (2012).

[83] M. G. Kozlov, M. S. Safronova, J. R. Crespo López-Urrutia, and P. O. Schmidt, Highly charged ions: Optical clocks and applications in fundamental physics, Rev. Mod. Phys. **90**, 045005 (2018).

[84] C. W. Gardiner and M. J. Collett, Input and output in damped quantum systems: Quantum stochastic differential equations and the master equation, Phys. Rev. A **31**, 3761 (1985).

[85] D. Barberena, R. J. Lewis-Swan, J. K. Thompson, and A. M. Rey, Driven-dissipative quantum dynamics in ultra-long-lived dipoles in an optical cavity, Phys. Rev. A **99**, 053411 (2019).

[86] J. A. Muniz, M. A. Norcia, J. R. Cline, and J. K. Thompson, A robust narrow-line magneto-optical trap using adiabatic transfer, arXiv:1806.00838.

[87] J. E. Sansonetti and G. Nave, Wavelengths, transition probabilities, and energy levels for the spectrum of neutral strontium (SrI), J. Phys. Chem. Ref. Data **39**, 033103 (2010).

[88] M. Scully and M. Zubairy, *Quantum Optics* (Cambridge University Press, Cambridge, 1997).

[89] V. Weisskopf and E. Wigner, Berechnung der natürlichen linienbreite auf grund der diracschen lichttheorie, Z. Phys. **63**, 54 (1930).